5

10

20

25

1

Fault inversion can accommodate ground deformation above inflating igneous sills

James Norcliffe[1], Craig Magee[2], Christopher A-L Jackson[1], Jonas Kopping[3], Bailey Lathrop[1]

[1]*Basins Research Group (BRG), Department of Earth Science and Engineering, Imperial College London, London, SW7 2BP, UK.*
[2]*School of Earth and Environment, University of Leeds, Leeds, LS2 9JT, UK.*
[3]*School of Earth, Atmosphere and Environment, Monash University, Melbourne, 3800, Australia.*

*Corresponding author: c.magee@leeds.ac.uk

ABSTRACT

Magma emplacement is commonly accommodated by uplift of the overburden and free surface. By assuming this deformation is purely elastic, we can invert the shape and kinematics of ground deformation to model the geometry and dynamics of underlying intrusions. However, magma emplacement can be accommodated by viscoelastic and/or inelastic processes. We use 3D seismic reflection data to reconstruct how elastic bending and inelastic processes accommodated emplacement of a Late Jurassic sill offshore NW Australia. We restore syn-emplacement ground deformation and compare its relief to sill thickness, showing that: (i) where they are equal, elastic bending accommodated intrusion; but (ii) where sill thickness is greater, inversion of a pre-existing fault and overburden compaction contributed to magma accommodation. Our results support work showing inelastic processes can suppress ground deformation, and demonstrate magmatism can modify fault displacements. Reflection seismology is thus powerful tool for unravelling links between magma emplacement, ground deformation, and faulting.

1 INTRODUCTION

Emplacement and inflation of sub-horizontal or inclined magma bodies (e.g., sills), particularly at shallow-levels, is commonly accommodated by uplift of the overlying rock and free surface [e.g., Biggs et al., 2011; Castro et al., 2016; Ebmeier et al., 2018; Galland, 2012b; Galland and Scheibert, 2013; Hansen and Cartwright, 2006; Johnson and Pollard, 1973; Pollard and Johnson, 1973; Schmiedel et al., 2017; Sigmundsson et al., 2020; Trude et al., 2003]. Where intrusion-induced uplift involves only elastic bending of the overburden, the shape and amplitude of the overlying fold produced (i.e. a 'forced fold') should broadly mimic the geometry and thickness of the underlying magma body [e.g., Bunger and Cruden, 2011; Hansen and Cartwright, 2006; Jackson et al., 2013; Pollard and Johnson, 1973; Stearns, 1978]. By assuming the host rock behaves elastically during magma emplacement we can analytically or numerically model ground

2

deformation patterns recorded in active volcanic areas; this may allow us to constrain possible intrusion geometries, locations, and dynamics [e.g., Biggs et al., 2009; Cannavò et al., 2015; Ebmeier et al., 2018; Pritchard and Simons, 2004; Sigmundsson et al., 2020; Sparks et al., 2012; van Wyk de Vries et al., 2014]. However, numerous studies have demonstrated that host rock deformation, in addition to elastic bending, may involve viscoelastic and/or inelastic (e.g.,

5   faulting or compaction) processes [e.g., de Saint-Blanquat et al., 2006; Guldstrand et al., 2017; Jackson et al., 2013; Magee et al., 2013a; Magee et al., 2019a; Magee et al., 2017; Morgan et al., 2008; Poppe et al., 2019; Schmiedel et al., 2019; Schmiedel et al., 2017; Schofield et al., 2012; Sigmundsson et al., 2020; Wilson et al., 2016]. These viscoelastic and inelastic processes can partly accommodate emplacement and thereby suppress the size of forced folds generated by elastic bending [e.g., Jackson et al., 2013; Magee et al., 2013a; Magee et al., 2019a]. The possible contribution of

10   viscoelastic and/or inelastic processes to accommodating magma emplacement means inversion of ground deformation patterns using elastic half-space models may thus underestimate key intrusion parameters (e.g., volume) [e.g., Galland, 2012b; Magee et al., 2018].

Although we recognise the need to better understand how magma emplacement translates into ground deformation [e.g.,

15   Ebmeier et al., 2018; Magee et al., 2018], most studies examine how intrusions create new structures (e.g., folds and faults) or modify host rock properties (e.g., porosity) [e.g., Hansen and Cartwright, 2006; Magee et al., 2019a; Montanari et al., 2017; Morgan et al., 2008; Reeves et al., 2018]. Here, we use 3D seismic reflection data from offshore NW Australia to investigate how pre-existing faults may affect the mechanics of roof uplift above an intruding sill. With these data we also explore how intrusion-induced deformation may modify fault displacement patterns, cautioning the

20   way we use such patterns to unravel fault kinematics in areas of co-located faulting and magmatism [e.g., Nicol et al., 1995; Nicol et al., 1996; Rotevatn et al., 2019; Walsh and Watterson, 1988]. We show that emplacement of the sill in the hanging wall of a major tectonic fault, at a depth of ~0.9 km during the Late Jurassic, was primarily accommodated by roof uplift facilitated by both local elastic bending and fault inversion. Local discrepancies between sill thickness and fold amplitude suggest other inelastic processes (e.g., porosity reduction) may have helped to generate space for the

25   intruding magma. Fault inversion locally reduced throw across the fault, which if not recognised as being intrusion-induced may be incorrectly interpreted as evidence of linkage between initially isolated fault segments [cf. Cartwright et al., 1995; Peacock and Sanderson, 1991]. Overall, our work demonstrates that seismic reflection data is a powerful tool for unravelling how intruding magma is expressed at the surface and interacts with faults.

30   2 GEOLOGICAL SETTING

The North Carnarvon Basin, located offshore NW Australia (Fig. 1A), formed through several phases of rifting between Australia and Greater India during the Late Carboniferous-to-Early Cretaceous [e.g., Direen et al., 2008; Gibbons et al.,

3

2012; Longley et al., 2002; Stagg et al., 2004]. Our study area is located within the Exmouth Plateau, a region of the North Carnarvon Basin containing <10 km thick, stretched continental crust and an up to 18 km thick sedimentary sequence (Fig. 1) [e.g., Exon et al., 1992; Karner and Driscoll, 1999; Pryer et al., 2002; Stagg et al., 2004]. To the north and west of the Exmouth Plateau are the Argo and Gascoyne abyssal plains, respectively, which consist of oceanic crust;

5   between the Exmouth Plateau and the Gascoyne Abyssal Plain is a 200–250 km wide continent-ocean transition zone comprising heavily intruded continental crust (Fig. 1A) [e.g., Direen et al., 2008; Symonds et al., 1998]. The Cuvier Abyssal Plain to the south-west, juxtaposed against the Exmouth Plateau by the Cape Range Fracture Zone, has traditionally been interpreted as oceanic crust, but may instead define an continent-ocean transition zone (Fig. 1A) [see Reeve, 2017 and references therein]. Several sub-basins (e.g., the Exmouth and Barrow sub-basins), each defined by a

10   unique tectono-stratigraphic evolution, lie east of the Exmouth Plateau (Fig. 1A) [e.g., Tindale et al., 1998].
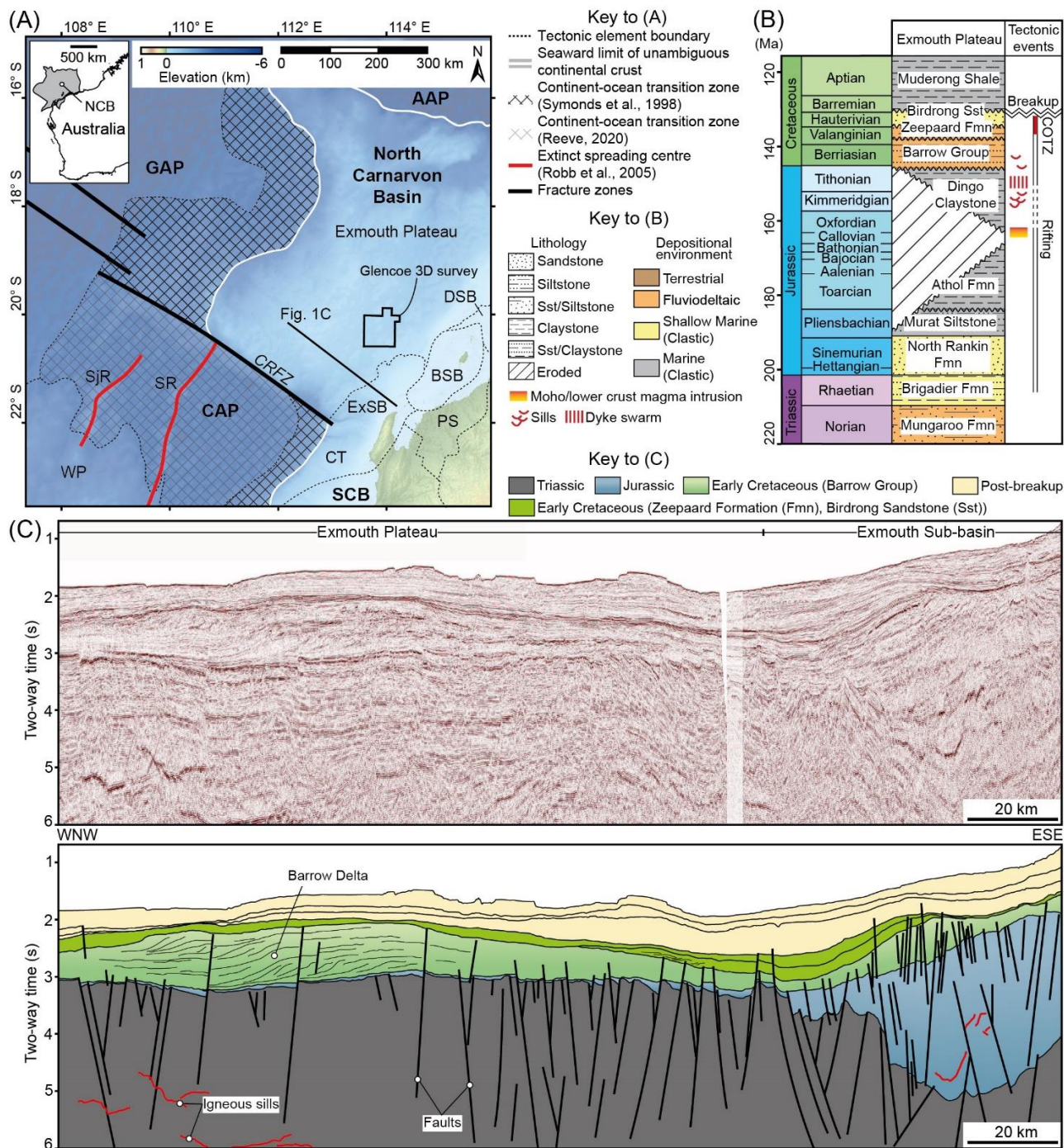
4

Figure 1: (A) Map of offshore NW Australia highlighting principal tectonic elements, including: NCB = North Carnarvon Basin, SCB = South Carnarvon Basin, ExSB = Exmouth Sub-basin, BSB = Barrow Sub-basin, DSB = Dampier Sub-basin, PS = Peedamullah Shelf, WP = Wallaby Plateau, CAP = Cuvier Abyssal Plain, GAP = Gascoyne Abyssal Plain,

AAP = Argo Abyssal Plain, SR = Sonne Ridge, SjR = Sonja Ridge, CRFZ = Cape Range Fracture Zone. Elevation data are based on the 2009 Australian Bathymetry and Topography grid (Geoscience Australia). (B) Stratigraphic column for the Exmouth Plateau summarising the age, dominant lithology, and generalised depositional environment for key units, as well as important tectonic and magmatic events [based on Hocking et al., 1987; Longley et al., 2002; Magee and Jackson, 2020; Tindale et al., 1998]. (C) Uninterpreted and interpreted 2D seismic line across the Exmouth Plateau and Exmouth Sub-basin. See Figure 1A for location.

The earliest phase of rifting on the Exmouth Plateau initiated in the Rhaetian (Late Triassic) and likely ceased towards the end of the Callovian (Middle Jurassic; Fig. 1B) [e.g., Bilal et al., 2018; Black et al., 2017; Gartrell et al., 2016; Tindale et al., 1998]. Late Triassic-to-Jurassic rifting produced an extensive array of ~N-S striking, high-throw (up to ~1 km) normal faults, which offset a thick pre-rift succession primarily consisting of fluvio-deltaic sedimentary rocks (i.e. the Mungaroo Formation; Figs 1B, C, and 2A) [e.g., Bilal et al., 2018; Black et al., 2017; Marshall and Lang, 2013; Stagg et al., 2004]. During the Early Jurassic, the Exmouth Plateau was sediment starved in comparison to the sub-basins located further east, resulting in deposition of a relatively condensed (≲100 m thick) latest Triassic-to-Early Jurassic, syn-rift succession (e.g., Fig. 1C) [e.g., Exon et al., 1992; Karner and Driscoll, 1999]. This syn-rift succession comprises the siliciclastic Brigadier and North Rankin formations, as well as the Murat Siltstone and Athol Formation, and records a transgression from shallow- to deeper-marine conditions (Fig. 1B) [e.g., Hocking, 1992; Hocking et al., 1987; Stagg et al., 2004; Tindale et al., 1998]. Development of a regional unconformity at the end of the Callovian marked the end of this first rift phase (Fig. 1B) [e.g., Bilal et al., 2018; Yang and Elders, 2016]. The unconformity is overlain by the marine Dingo Claystone (Oxfordian-to-Tithonian; Fig. 1B) [e.g., Tindale et al., 1998].
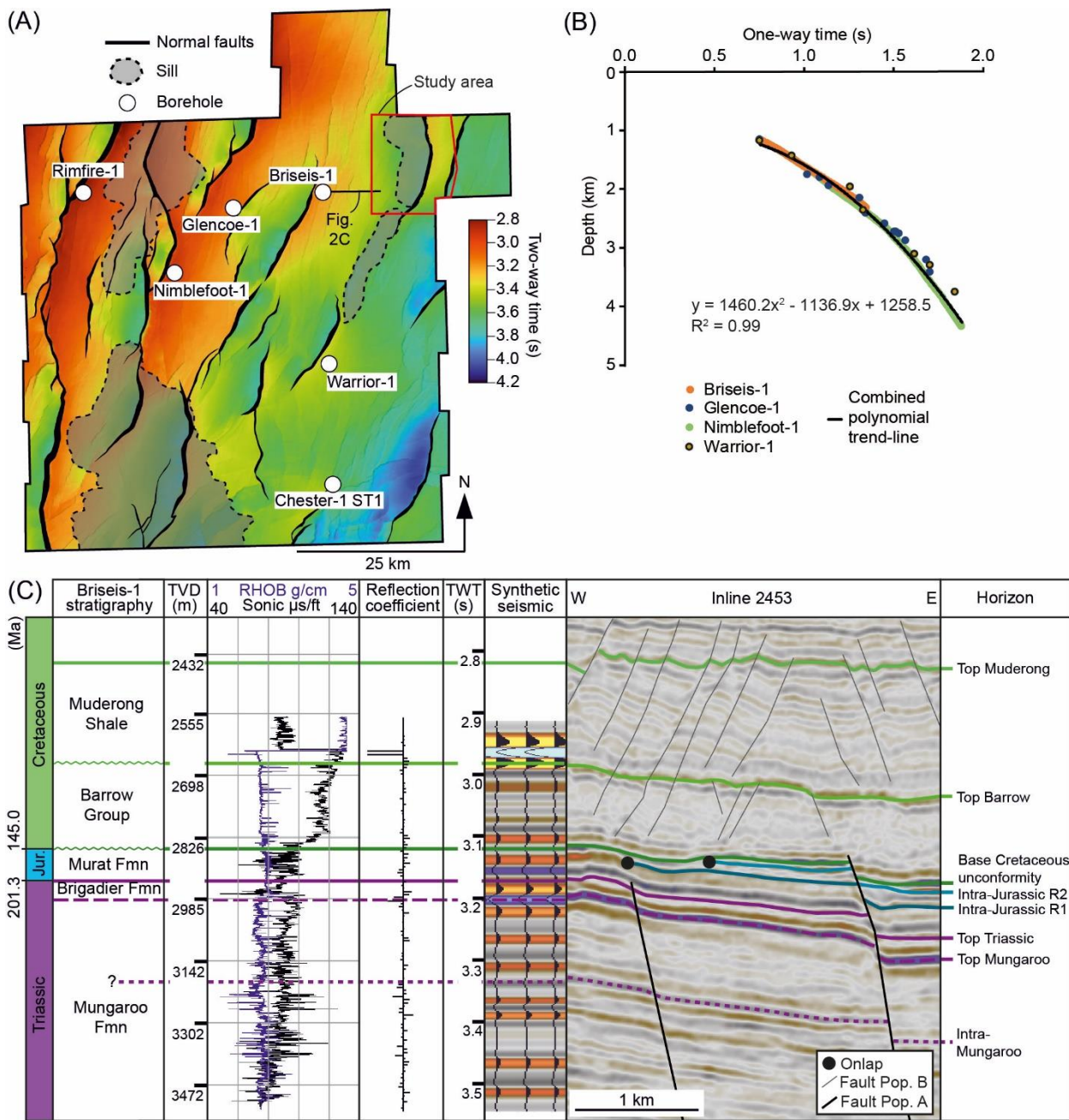
6

Figure 2: (A) Time-structure map of the Top Mungaroo horizon showing borehole locations and major tectonic normal faults. See Figure 1A for location. (B) Time-depth plot for borehole data from Briseis-1, Glencoe-1, Nimblefoot-1, and Warrior-1. A second-order polynomial trend-line is plotted through all data to define the time-depth relationship. (C) Borehole data from Briseis-1 and associated synthetic seismic trace compared to the actual seismic data (see Fig. 2A for line location). Mapped horizons and fault populations (pop.) highlighted.

7

Crustal extension is broadly considered to have continued throughout the Jurassic across the North Carnarvon Basin [e.g., Gartrell et al., 2016; Tindale et al., 1998], although the apparent cessation of faulting during deposition of the Dingo Claystone on the Exmouth Plateau suggests rifting may have been punctuated by a period of tectonic quiescence (Fig. 1B) [e.g., Magee et al., 2016]. Development of the Base Cretaceous unconformity at ~148 Ma (latest Tithonian) and subsequent rapid subsidence to accommodate a thick succession of deltaic rocks (i.e. the Tithonian-to-Valanginian Barrow Group), mark the onset of a second rift phase across the Exmouth Plateau (Figs 1B and C) [e.g., Paumard et al., 2018; Reeve et al., 2016]. Tithonian-to-Valanginian rifting involved relatively little upper crustal faulting, with this event producing an array of N-S to NE-SW-striking, low-throw (<0.1 km) normal faults. It is thus likely that stretching during this period was dominated by depth-dependent extension or dynamic topography [e.g., Driscoll and Karner, 1998; Reeve et al., 2016]. Rifting culminated in the development of an continent-ocean transition zone and ultimately continental break-up along the western margin of the Exmouth Plateau in the Valanginian-to-Hauterivian (~135–130 Ma; Fig. 1B) [e.g., Direen et al., 2008; Robb et al., 2005; Stagg et al., 2004]. Following continental break-up in the Early Cretaceous, thermal subsidence controlled margin development, resulting in the development of a thick post-rift succession, parts of which have been deformed by tiers of polygonal faults (e.g., Fig. 1C) [e.g., Paganoni et al., 2019; Velayatham et al., 2019].

The North Carnarvon Basin records a complex and protracted history of magmatic activity during the Late Jurassic-to-Early Cretaceous (Fig. 1B). A mafic-to-ultramafic, high-velocity magmatic body was emplaced in the lower crust, possibly during the Middle Jurassic, which may have promoted regional uplift and formation of the Callovian unconformity [e.g., Frey et al., 1998; Rey et al., 2008; Rohrman, 2013; Rohrman, 2015]. Extensive sill-complexes across the North Carnarvon Basin (e.g., Fig. 2A), which dating of intrusion-induced forced folds and vent complexes indicate were emplaced at least during the Kimmeridgian, may have been fed by this high-velocity magmatic body [e.g., Frey et al., 1998; Magee et al., 2013a; Magee et al., 2017; Rey et al., 2008; Rohrman, 2013]. A transition from sill-complex emplacement to intrusion of an extensive dyke swarm occurred at ~148 Ma, coincident with formation of the Base Cretaceous unconformity [Magee and Jackson, 2020]. The last and main phase of magmatism across the North Carnarvon Basin resulted in development of the continent-ocean transition zones and associated volcanics during break-up (e.g., seaward-dipping reflectors), as well as sporadic sill intrusions within the basin interior [e.g., Hopper et al., 1992; Magee et al., 2013b; Mark et al., 2020; Rey et al., 2008; Symonds et al., 1998].

3 DATA AND METHODS

8

3.1 Data

Here we use the publicly available, high-quality, time-migrated Glencoe 3D seismic reflection survey that was acquired by CGGVeritas in 2007-2008 (Figs 1A and 2A). Data were recorded with a line spacing of 25 m using 10, 6 km long streamers, with 480 channels recording to ~8 s two-way time (TWT) at a sample interval of 2 ms. The seismic source had a volume of 3460 in^3 and was fired at shot point intervals of 12.5 m at a tow depth of 7 m. Full-fold, the dataset covers an area of approximately 4042 km^2 (Fig. 2A). Seismic data were processed to zero-phase and are here displayed with SEG standard polarity, whereby a downward increase in acoustic impedance corresponds to a peak (red-to-yellow on seismic sections) and a downward decrease in acoustic impedance as a trough (blue or black on seismic sections).

We use data from the Briseis-1, Nimblefoot-1, Warrior-1, and Glencoe-1 boreholes to determine (Fig. 2): (i) the age of the mapped horizons and the lithology (and age) of the stratigraphic units they bound; and (ii) a time-depth relationship, constrained by checkshot data, which allows us to depth-convert measurements within the sedimentary sequence from seconds two-way time to metres (Fig. 2B; Supplementary Table 1). By measuring the dominant wavelength ($\lambda = 26.3$ m) of stratal seismic reflections in the interval of interest, we estimate that the limit of separability ($\lambda/4$; where λ is the seismic wavelength) and visibility ($\lambda/30$) for the sedimentary succession are ~6.6 and ~0.9 m, respectively.

No boreholes intersect the igneous intrusion within our study area, but data from the nearby Rimfire-1 and Chester-1 ST1 wells (Fig. 2A), which intersect a ~10 m thick intrusion and an ~18 m wide dyke respectively, suggests intrusions in the region are likely mafic [Childs et al., 2013; Magee and Jackson, 2020; Moig N and Massie, 2010]. Although there is no velocity information available for the thin intrusions intersected by Rimfire-1 and Chester-1 ST1, we consider the sill we study has a seismic velocity of ~5.55($\pm$0.555) km s^{-1}; this range is based on velocity data acquired from mafic intrusions in other sedimentary basins [e.g., Magee et al., 2019a; Skogly, 1998; Smallwood and Maresh, 2002]. At the level of the intrusion in our study area, the dominant frequency of the data is ~25 Hz, which coupled with a seismic velocity of ~5.55($\pm$0.555) km s^{-1} suggests the limits of separability and visibility for the sill are ~56($\pm$5.6) m and ~7($\pm$0.7) m, respectively. Where the sill has a thickness between these limits of separability and visibility, it is expressed in the data as a tuned reflection package; i.e. seismic energy reflected from the top and base intrusive contacts combines on its return to the surface and cannot be deconvolved [e.g., Eide et al., 2018; Smallwood and Maresh, 2002]. Where the sill is thicker than the limit of separability, its top and base reflections can be distinguished, allowing us to use our inferred velocity range to depth-convert the intrusions measured thickness from seconds TWT to metres.

3.2 Methods

3.2.1 Seismic Interpretation

To define the geometry of the studied sill, which around its outer edges typically appears as a tuned reflection package, we mapped two seismic horizons (Top and Base Sill). We also mapped eight seismic horizons within the host sedimentary sequence to provide a seismic-stratigraphic framework for our analyses. Biostratigraphic data from the Briseis-1 borehole, which is closest to the study area, provides direct age constraints on five mapped horizons (Fig. 2C): (i) Top Muderong (~113 Ma); Top Barrow Group (~138 Ma); Base Cretaceous unconformity (~148 Ma); Top Triassic (~201 Ma); and Top Mungaroo (near Norian–Rhaetian boundary; ~208 Ma). Four of these biostratigraphically dated horizons were tied to the seismic reflection data by creation of a synthetic seismogram for the Briseis-1 well-log data; well-logs only extend between depths of 2563–3548 m TVD (total vertical depth beneath the drill floor) and thus do not intersect the Top Muderong horizon (Fig. 2C). The location of the Top Muderong was instead constrained by using checkshot data from Briseis-1 to convert the measured depth of the horizon in metres to TWT (Fig. 2B). In addition to the five dated horizons we mapped an intra-Mungaroo Formation horizon encountered in Briseis-1, but for which the exact age remains unconstrained (i.e. Intra-Mungaroo; Fig. 2C). We also mapped two horizons above the Top Triassic, but these could not be dated as they were eroded by the Base Cretaceous unconformity and do not extend to the location of Briseis-1; we term the stratigrapically oldest of these horizons Intra-Jurassic R1, and the other Intra-Jurassic R2 (Fig. 2C). All horizons were mapped across the study area, except for the Intra-Mungaroo horizon, which was only identified locally as sub-sill imaging often hindered its recognition. Thickness maps (isochores) between various combinations of the mapped horizons were used to assess deformation of the sedimentary sequence through time.

3.2.2 Forced fold analysis

If the emplacement of a sub-horizontal, tabular magma body (e.g., a sill) is fully accommodated by elastic bending, we may expect the intrusion thickness ($ST0$) to equal the syn-intrusion amplitude ($F0$) of the resultant fold (Fig. 3A) [e.g., Bunger and Cruden, 2011; Galland and Scheibert, 2013; Goulty and Schofield, 2008; Hansen and Cartwright, 2006; Pollard and Johnson, 1973]. However, if inelastic processes (e.g., compaction) also contribute to generating space for intruding magma, and thus suppress uplift, we may expect $ST0>F0$ (Fig. 3B) [e.g., Jackson et al., 2013; Magee et al., 2013a; Magee et al., 2019b; Schmiedel et al., 2017]. We calculate the present-day, vertical fold amplitude (F) every 10 m along a representative seismic line by measuring and depth-converting the distance between the top fold horizon and a projected pre-fold datum (Fig. 3) [e.g., Hansen and Cartwright, 2006]. We also calculate the present-day, vertical sill thickness (ST) every 10 m along the same profile and compare this to F (Fig. 3). Because burial-related compaction likely reduces fold amplitude through time (i.e. $F0>F$; Figs 3C and D), without affecting the thickness of typically

10

incompressible intrusions (i.e. we assume T=T0), we backstrip and decompact F to estimate F0 (Figs 3C and D) [e.g., Magee et al., 2019a].
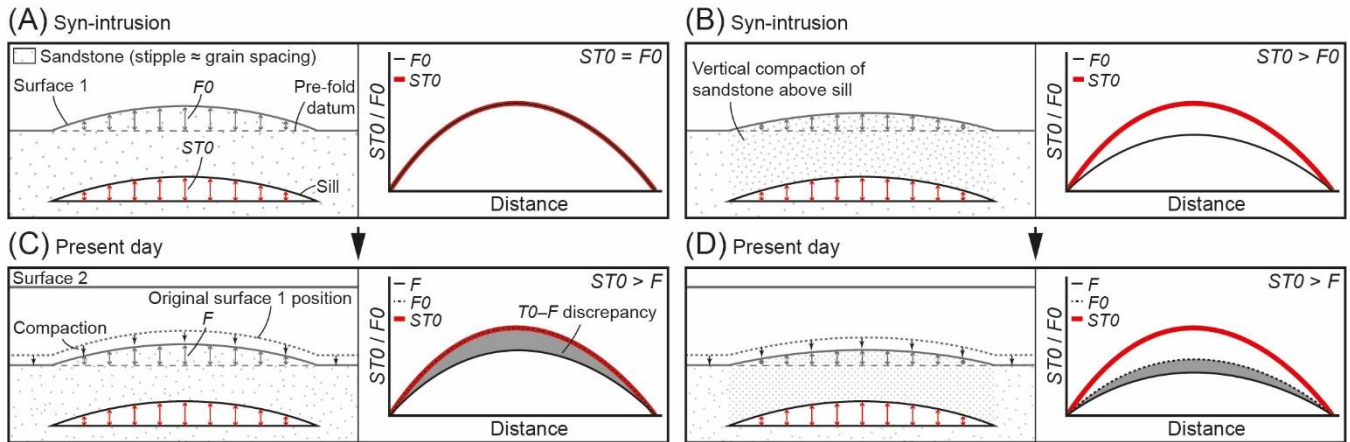
Figure 3: (A) Schematic showing uplift above a sill if accommodated purely by elastic bending of a sandstone overburden. A plot of showing how original sill thickness (T0) and fold amplitude (F0), based on defining a pre-fold datum, change with distance from left to right is included; note T0 and F0 are equal. (B) Schematic showing uplift above a sill if vertical compaction of the overburden accompanies elastic bending; F0 is less than T0 across the profile. (C and D) Schematics of (A) and (B) following burial-related compaction, respectively. In both cases, the present-day fold amplitude (F) is less than T0.

Airy backstripping of strata involves restoration of its initial porosity (ϕ_0) by removing the effects of overburden loading [e.g., Sclater and Christie, 1980], and thus requires knowledge of: (i) the current porosity (ϕ) of a given sedimentary sequence; and (ii) the compaction length scale (λ), which is the inverse of the compaction coefficient and estimates the rate of compaction with increasing burial depth. Given that no boreholes penetrate the entire folded sequence, either at the actual fold or elsewhere in the 3D survey, we could not estimate ϕ and λ from our data. Instead, following the method outlined by Magee et al. [2019a], we computed an envelope of potential backstripped *F0* using a range of realistic ϕ_0 (0.7–0.25) and λ (3.7–1.4) values for claystones and sandstones as these rock types dominate the folded siliciclastic sequence studied (e.g., Fig. 1B).

There are several limitations to our method for comparing *ST0* and *F0*. First, we assume that the measured sill thickness (ST) is equal to *ST0* (Fig. 3), but acknowledge that post-emplacement magma expulsion and/or contraction during crystallisation could mean *T<ST0* [e.g., Caricchi et al., 2014; Chaussard, 2016; Magee et al., 2019a]. The use of incorrect seismic velocities may also introduce imprecision into our depth-conversion of *ST* and *F*, although we consider that the

11

range of velocities used for the sill and those for the borehole-constrained folded stratigraphy minimises this error. However, our method does not account for potential lateral variations in seismic velocity across the sill or forced fold, which could reflect changes in lithology. Finally, we note that the Airy backstripping method applied assumes the folded layers had no flexural strength (i.e. elastic thickness) [Magee et al., 2019a]. Yet if the folded rock layer had an elastic thickness, its fold amplitude would have been suppressed [e.g., Hardy and Finch, 2006; Oehlers et al., 1994]. We note that folding of a layer with a flexural strength would promote lengthening of the fold beyond the limits of the underlying forcing mechanism (i.e. the sill); our assumption that the folded sequence has no flexural strength may thus be partially validated by an observed coincidence between the fold outline (i.e. where fold amplitude is zero) and the sill edge [Hansen and Cartwright, 2006; Magee et al., 2019a]. Overall, whilst these limitations my cause *F0* to deviate from *ST0*, we consider their effects are likely negligible and suggest that a difference between *ST0* and *F0* of >5% can probably be related to syn-emplacement processes, as opposed to post-emplacement modification of *ST0* or simply reflecting measurement errors [Magee et al., 2019a].

3.2.3 Fault kinematics

To establish the geometrical and kinematic relationships between the sill, its overlying forced fold, and faulting, we conducted throw analysis of the major, N-S striking, W-dipping fault (Fault 1) that borders the eastern edge of the sill. Throw-depth (*T-z*) and throw-distance (*T-x*) profiles are commonly used to assess the geometry and infer the kinematics of normal faults [e.g., Baudon and Cartwright, 2008; Hongxing and Anderson, 2007; Jackson et al., 2017; Rotevatn et al., 2019]. For example, local throw minima expressed in *T-x* profiles may represent breached relays formed during fault segment linkage [e.g., Cartwright et al., 1996; Mansfield and Cartwright, 1996; Peacock and Sanderson, 1991]. Furthermore, changes in throw gradient (in *T-z* or *T-x* profiles) can help identify intervals containing syn-tectonic growth strata, which thus constrain periods of active faulting [e.g., Ferrill and Morris, 2001; Walsh and Watterson, 1989]. Although we were not able to identify piercing points (e.g., channels) either side of Fault 1 to establish whether there was any along-strike offset of strata, we assume faulting was dip-slip and that measured throw patterns reflect displacement distribution.

We compiled a throw-depth plot for a representative seismic line crossing Fault 1, near its centre, by measuring the vertical offset of each mapped horizon. Where horizons adjacent to Fault 1 appear deflected, we projected their regional trend to define the fault cut-off and thereby account for both brittle and ductile strains [e.g., Mansfield and Cartwright, 1996]. We extracted expansion indices (EI) from the same line; EI reflect the difference between the hanging wall and footwall thickness of a given stratal package [e.g., Cartwright et al., 1998; Jackson et al., 2017; Thorsen, 1963]. These quantitative fault measurements allow us to constrain the main periods of fault activity, as well as temporal variations in

12

the relative rates of sediment accumulation and fault-throw, at least in two-dimensions [e.g., Jackson et al., 2017]. We analysed along-strike variations in fault throw (*T-x*) by measuring Top Mungaroo hanging wall and footwall cut-offs every 100 m along Fault 1 on sections oriented normal to the fault; we selected this horizon for *T-x* analysis because it is well-imaged and occurs at a similar stratigraphic level to the sill. To assess the relationship between sill thickness and

5   fault throw, we also measured sill thickness in the hanging wall of the fault, on the same profiles, every 100 m along-strike.

4 Sill-fault-fold geometry and spatial relationships

4.1 Sill characterisation

10   The studied sill comprises a >13.4 km long, N-trending, strata-concordant inner sill, bound on its eastern and most of its western flanks by inwardly inclined sheets, and located within the Mungaroo Formation (Fig. 4). The Top Sill contact corresponds to a high-amplitude, positive reflection, marking a downward increase in acoustic impedance across the sedimentary strata-sill interface, and currently occurs at a maximum depth of ~3.81 s TWT (Figs 4A, D, and E). Across much of this inner sill, we identify and map a discrete Base Sill reflection, which has a high-amplitude and negative

15   polarity (i.e. it marks the downward decrease in acoustic impedance; Figs 4B, D, and E). Within the southern and north-western sector of the inner sill, we observe no discrete Base Sill contact and the sill is instead expressed as a tuned reflection package; in these areas we map the Base Sill as the lowermost reflection in the tuned package but note this may not correlate to the true base sill contact (e.g., Figs 4B, D, and E). Along its eastern margin and the southern ~7.2 km of its western edge, the sill transitions into transgressive, inward-dipping inclined sheets, which also correspond to

20   tuned reflection packages (Fig. 4). Each inclined sheet extends up into the overlying Jurassic succession, but appear to terminate below Intra-Jurassic R1 horizon (e.g., Fig. 4B). The eastern inclined sheet coincides with a major, N-S striking, W-dipping, tectonic fault (Fault 1; Fig. 4). Where both eastern and western inclined sheets are developed, the entire sill is relatively narrow (up to 4.8 km wide) and the inner sill is ≲3.2 km wide (Fig. 4). North of this zone, where there is no western inclined limb, the sill abruptly widens (up to 6.4 km wide) and has a convex-outwards, lobate western

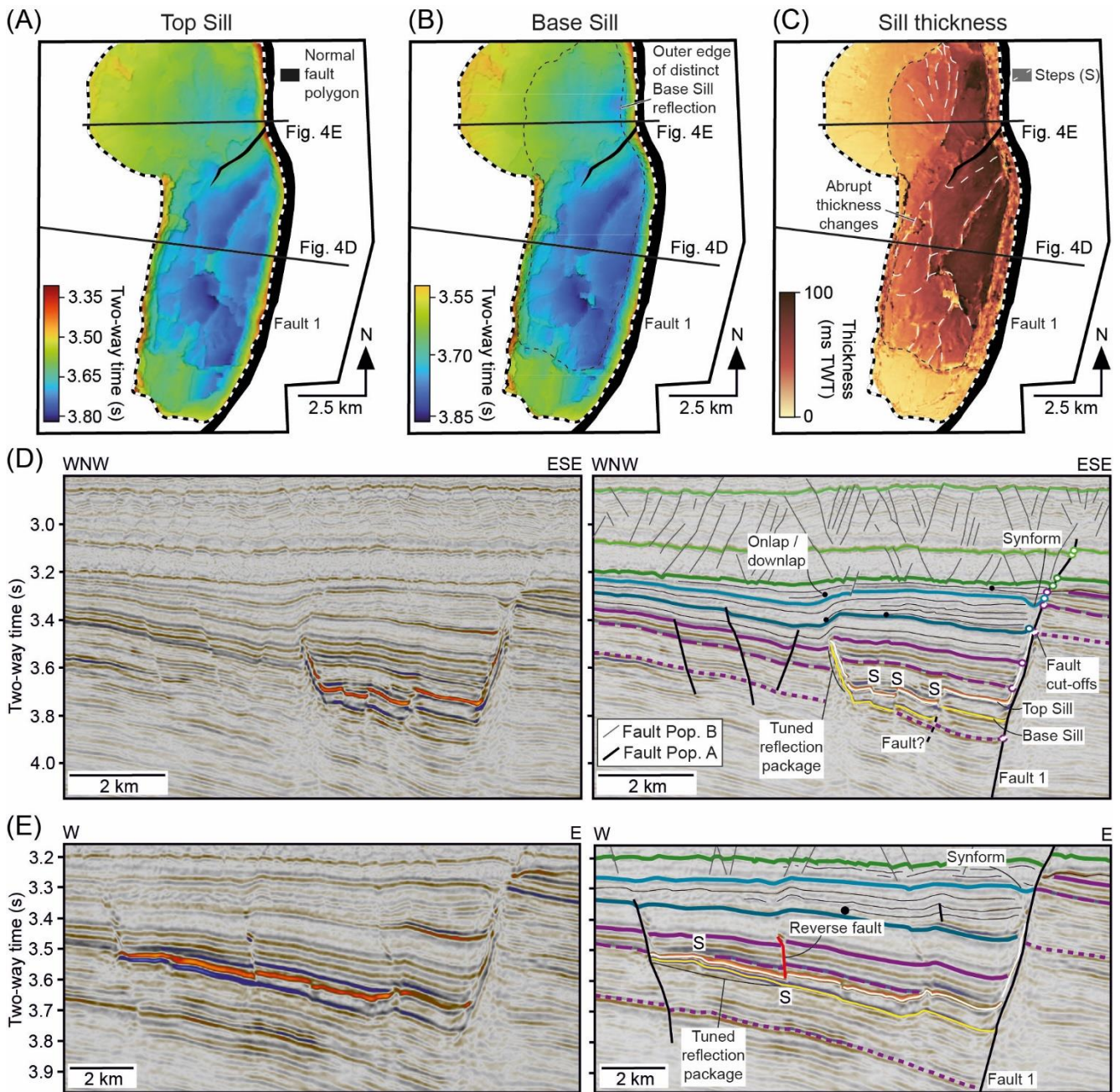25   termination (Figs 4A-C and E).

13

Figure 4: (A-C) Maps showing the time-structure of the Top (A) and Base (B) sill horizons, as well as the vertical thickness (C) difference (in time) between them. The Base Sill horizon was only mapped where it could be distinguished as a distinct reflection. (D and E) Uninterpreted and interpreted seismic sections detailing the sill geometry and associated host rock deformation. See Figure 4A-C for locations and Figure 2C for horizon key.

14

Distinguishing discrete Top Sill and Base Sill reflections across much of the inner sill allows us to assess vertical sill thickness in metres (Fig. 4C; e.g., Supplementary Table 2). We show the inner sill is locally up to ~98 ms TWT (~272±27 m) thick (Fig. 4A). In the eastern half of the intrusion where the inner sill is bound by Fault 1, its thickness varies between

5 ~60–90 ms TWT (~166±17 m to 249±25m), broadly decreasing westwards to 40–60 ms TWT (~111±11 m to 166±17m) (Fig. 4A). The inclined sheets, as well as the southern inner sill tip and its arcuate westwards termination, are expressed as tuned reflection packages, such that their thickness can only be defined as being between the limits of separability (56±5.6 m) and visibility (~7±0.7 m) for the data (e.g., Figs 4B and C). Across the inner sill we recognise discrete and abrupt changes in thickness where (Fig. 4C): (i) the Top Sill and Base Sill reflections become tuned; and (ii) vertical

10 offsets (steps) in the Top Sill and Base Sill reflections occur (see also Fig. 4D).

4.2 Stratigraphic framework and forced fold characterisation

The Top Mungaroo horizon dips eastwards towards Fault 1 (Figs 4D, 4E, and 5A). Local, abrupt changes in Top Mungaroo depth are observed across the study area where the horizon (Fig. 5A): (i) is offset by up to ~0.5 s TWT across minor, ~NE-SW striking normal faults (Fault Population A); and (ii) overlies or is cross-cut by the western edge of the

15 sill. Although the underlying Intra-Mungaroo horizon cannot be mapped fully across the study area, where identified, it broadly parallels the Top Mungaroo horizon (e.g., Figs 4D and E). In most places the Intra-Mungaroo horizon is located >0.75 s TWT beneath the Top Mungaroo horizon, except where it extends beneath the sill and the Top Mungaroo is locally uplifted (e.g., Figs 4D and E).
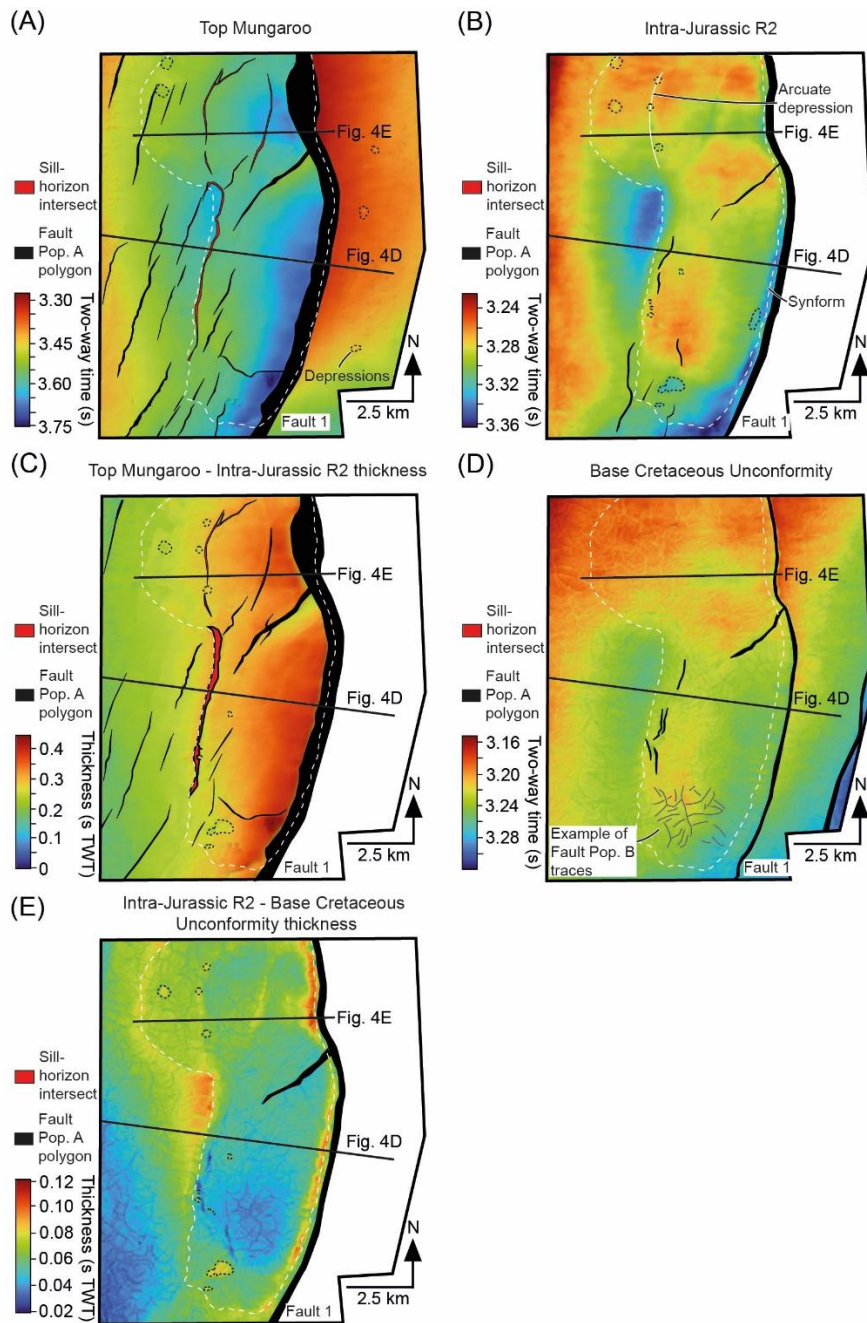
15

Figure 5: (A) Time-structure map of the Top Mungaroo horizon showing Fault Population (Pop.) A polygons and sill outline. See Figure 2A for location. (A) Time-structure map of the Intra-Jurassic R2 horizon. (C) Vertical thickness (in time) between the Top Mungaroo and Intra-Jurassic R2 horizons. (D) Time-structure map of the Base Cretaceous unconformity. Some Fault Population B traces interpreted; others omitted for clarity. (E) Vertical thickness (in time) between the Intra-Jurassic R2 and Base Cretaceous unconformity horizons.

16

Intra-Jurassic R2 is only observed in the hanging wall of Fault 1, where it is locally offset by faults within Fault Population A (Fig. 5B). Uplift of supra-sill horizons, relative to their projected regional trends, is clearly demonstrated by Intra-Jurassic R2 where the margins of a dome-shaped fold directly overlie the western and eastern lateral tips of the

5   sill (Figs 4D, E, and 5B). The western margin of the dome-shaped fold is a W-verging monocline, which includes folded strata between the Top Triassic and Intra-Jurassic R2, whereas its eastern margin has a subtle synformal geometry immediately adjacent to Fault 1 that is only expressed between Intra-Jurassic R1 and R2; below Intra-Jurassic R1 there is no apparent folding of horizons adjacent to Fault 1 (Figs 4D, E, and 5C). Above the deepest part of the Top Sill horizon (i.e. ~3.81 s TWT), the Intra-Jurassic R2 horizon is currently located at ~3.25 s TWT. Superimposed onto the dome-

10   shaped fold at the Intra-Jurassic R2 level are three broad areas of elevated relief (up to ~3.26 s TWT), separated by subtle lows (~3.30 s TWT; Fig. 5B). Within the northern-most region of elevated relief is a thin narrow (<100 m wide), arcuate depression that extends for ~3 km along strike and coincides with an apparent reverse fault (Figs 4E and 5C). Numerous sub-circular and elliptical, ≲1 km wide, ≲0.2 s TWT deep depressions are observed within the dome-shaped fold towards its western margin along Intra-Jurassic R2 (Figs 5B and C). Between the Top Mungaroo and Intra-Jurassic R2 horizons,

15   there is a general thickening of strata towards Fault 1 (Fig. 5C); this thickening in part relates to the presence of stratigraphic reflections extending westwards from Fault 1 that onlap onto Intra-Jurassic R1 (e.g., Fig. 4C). There is no apparent change in this regional thickening trend of the Top Mungaroo-to-Intra-Jurassic R2 strata above the western edge of the sill (Fig. 5C). Where depressions are observed at Intra-Jurassic R2 and/or the Top Mungaroo, the intervening strata is locally thinner than adjacent areas (Fig. 5C).

20

The clear dome-shaped fold observed at Intra-Jurassic R2 and its internal variations in elevation are subtly expressed across the Base Cretaceous unconformity (Fig. 5D). Compared to deeper stratigraphic horizons, offset (up to ~0.1 s TWT) of the Base Cretaceous unconformity across Fault 1 is reduced and very minor changes in depth define a polygonal pattern (Fig. 5D). Strata between Intra-Jurassic R2 and the Base Cretaceous unconformity display complex thickness

25   variations (Fig. 5E): (i) there is a broad thickening towards Fault 1, interrupted by the dome-shaped fold across which strata is relatively thin (~0.04–0.09 s TWT); (ii) a zone of thickening parallel to Fault 1 above the eastern sill tip, and overlying the synform developed along Intra-Jurassic R2; and (iii) localised zones of thickening, overlying the sub-circular depressions on Intra-Jurassic R2. The thinning of strata bound by the Intra-Jurassic R2 and Base Cretaceous unconformity horizons across the dome-shaped fold is accommodated by the onlap of reflections onto the fold limbs

30   (e.g., Fig. 4B).

17

4.2.1 Comparison between sill thickness and fold amplitude

We compare the present-day vertical sill thickness (*ST*), which we consider equal to *ST0*, and fold amplitude (*F*) at Intra-Jurassic R2 along a selected seismic section (i.e. Fig. 4B) where the sill is ~4.5 km wide (Fig. 6; Supplementary Tables 2 and 3). We show *ST* ranges from 56(±5.6) m at the edges of the inner sill to a maximum of ~259(±26) m (Fig. 6; Supplementary Table 2); note we only measure *ST* where the top and base sill contact reflections can be defined and thus do not take into account the tuned reflection packages defining the inclined sheets. The *ST* profile can be sub-divided into four parts [i-iv] where *ST* is relatively stable, separated by abrupt increases and decreases in *ST* (Fig. 6); *ST*mean of these parts decreases westwards from ~204(±20) m to ~150(±15) m, respectively (Fig. 6). The marked changes in *ST* correspond to where steps occur within the sill reflection(s) (Figs 4B and 6).
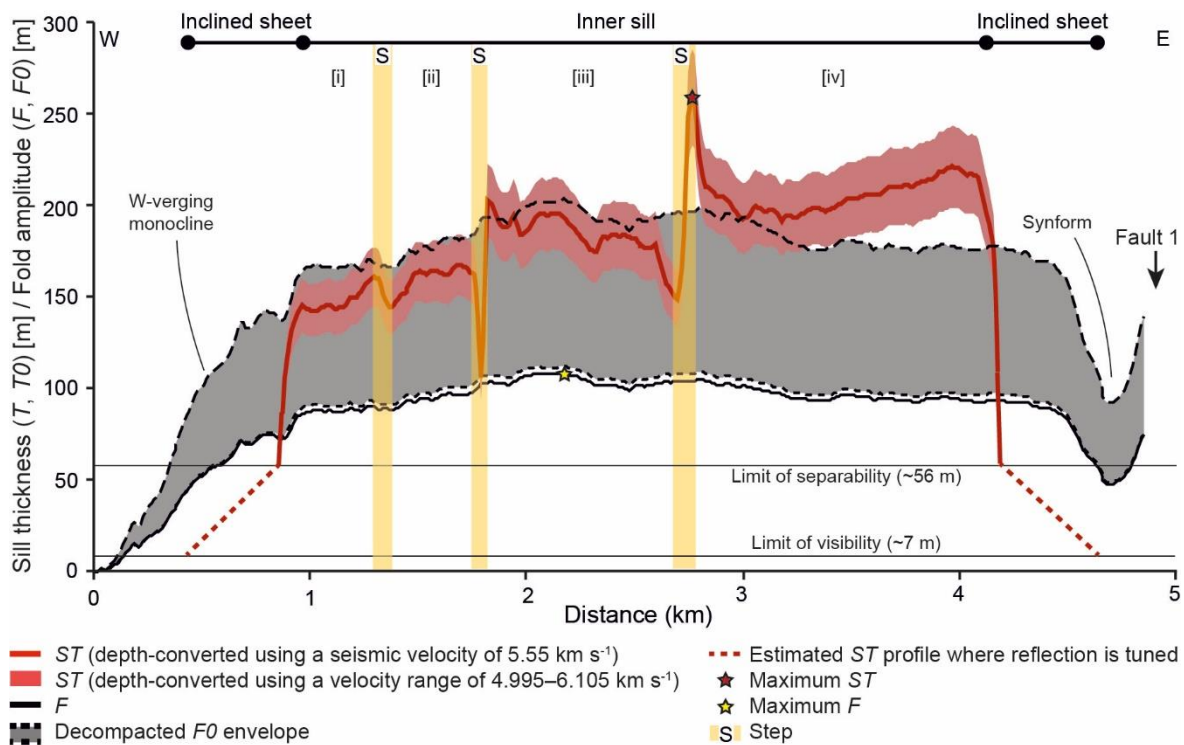

Figure 6: Plot of sill thickness and fold amplitude changes across the seismic line shown in Figure 4B. Sill thickness (*ST*) is assumed to equal the original sill thickness (*ST0*) and its measurements in time have been depth-converted to metres assuming a seismic interval velocity of ~5.55(±0.555) km s^{-1}. Sill thickness was only measured across the inner sill where a distinct Base Sill horizon can be mapped (e.g., Figs 4D and E). The thickness of the inclined sill limbs, which appear as tuned reflection packages in the seismic data, can only be defined as being between the limits of separability and visibility. The present-day fold amplitude (*F*) was measured in time and converted using borehole-

18

constrained seismic velocities. We decompacted and backstripped F using a range of parameters to estimate the possible original fold amplitude ($F0$), which we display as an envelope.

Along the selected seismic section, the fold is ~4.8 km wide, extending slightly to the east and west of the underlying sill tips (Figs 4B and 6). The fold has a relatively flat top and is defined by a W-verging monocline on its western limb (Figs 4B and 6). On its eastern limb, the fold has a synformal geometry (Figs 4B and 6); i.e. at the fault, the present-day fold amplitude (F) is ~75 m but above the eastern edge of the sill, which underlies the synform fold axis, F is ~47 m (Fig. 6; Table 2). Along the profile, the maximum measured F of ~116 m is ~54(±5)% less than the maximum ST (i.e. 259(±26) m) and the two areas are laterally offset by ~0.59 km in 2D (Fig. 6; Supplementary Tables 2 and 3). Overall, $ST>F$ by an average of ~37(±7)%, except where the inner sill transitions to the inclined sheets and across one of the sill steps (Fig. 6). We observe no marked variations in F where the sill appears stepped (Fig. 6).

We backstripped our measured F profile, using a range of ϕ_0 and λ parameter values, to define an envelope bounding $F0$ (Fig. 6; Supplementary Table 3). Our backstripped $F0$ envelope mirrors the geometry of the measured F profile, but has a greater magnitude (Fig. 6). For example, backstripping suggests the maximum $F0$ is between ~112–205 m, which is ~2–95 m greater than F (Fig. 6); these values suggest the maximum $F0$ was less than the maximum ST by ~57(±7)–21(±7)%. Across most of the fold there is an overlap between ST and $F0$ envelopes, although T in the eastern section of the sill is locally greater than $F0$ (Fig. 6). Where the Intra-Jurassic R2 horizon displays a synformal geometry above the eastern sill edge, the backstripped relief of the synform fold axis above the assumed pre-fold datum is ~48–92 m and at Fault 1 it is ~75–139 m (Fig. 6).

4.3 Fault characterisation

Two fault populations are observed (Figs 4 and 5). Fault Population A comprises an array of N-to-NE striking, low-to-high throw normal faults primarily located within Triassic-to-Jurassic strata (Figs 4 and 5). Several faults within Population A offset the Base Cretaceous unconformity and extend upwards into the overlying sedimentary sequence (e.g., Figs 4B and C). Fault Population A does not appear to offset the sill (Fig. 4). Fault Population B is located primarily within the Early Cretaceous Barrow Group and Muderong Formation; faults within this population rarely extend below the Base Cretaceous Unconformity (e.g., Figs 4B and C). Faults within Fault Population B are closely spaced, have low-throws (≤25 ms TWT), a normal sense of motion, and are arranged in a polygonal pattern (Figs 4B, C, and 5E).

Fault 1 bounds the eastern edge of the sill and is part of Fault Population A (e.g., Figs 4B and C). There is a minor NNW-trending bend in Fault 1 where it is intersected in its hanging wall by a ~3 km long, NW-dipping splay fault (Fig. 5). A

19

T-z analysis of Fault 1 reveals throw decreases upwards from ~426 ms TWT at the Intra-Mungaroo horizon to ~0.02 ms TWT at the Top Barrow, just below its upper tip (Fig. 7A; Supplementary Table 4). Superimposed on this throw are three zones between (Fig. 7A; Supplementary Table 4): (i) the Intra-Mungaroo and Top Triassic horizons, where the throw gradient (i.e. change in throw divided by change in depth) is relatively low (~0.49); (ii) the Top Triassic and Base Cretaceous Unconformity horizons, where the throw gradient is relatively high (~1.59); and (iii) the Base Cretaceous unconformity and upper fault tip, where the throw gradient is again relatively low (~0.32). For the Intra-Mungaroo-to-Top Mungaroo strata, an expansion index of 1.59 suggests the sequence thickens across the fault (Fig. 7A; Supplementary Table 5). However, this expansion index does not consider the thickness of the sill emplaced within the hanging wall portion of the Intra-Mungaroo-to-Top Mungaroo strata; if sill thickness is accounted for, the true expansion index for this unit is 1.04 (Fig. 7A). The expansion index for the Top Mungaroo-to-Top Triassic, which should be considered a minimum estimate because the Top Triassic is eroded in the footwall and the basin was sediment-starved during this period, is 1.61 (Fig. 7A; Supplementary Table 5). We cannot calculate an expansion index for Intra-Jurassic R1-to-Intra-Jurassic R2 or Intra-Jurassic R2-to-Base Cretaceous unconformity strata because these horizons are not present in the footwall (e.g., Figs 4B and 7A). Above the Base Cretaceous unconformity, expansion indices are <1.26 (Fig. 7A; Supplementary Table 5).
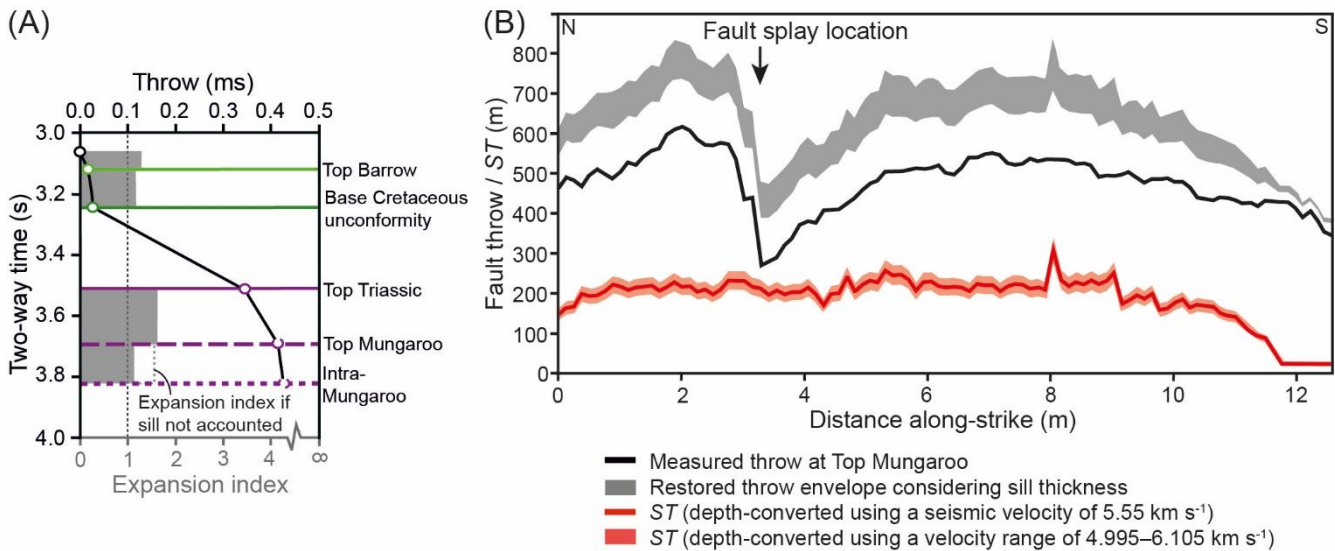

Figure 7: (A) Throw-depth (*T-z*) plot compiling measurements from all horizons observed in both the hanging wall and footwall of Fault 1 along the seismic section in Figure 4B. Expansion indices for each interval are also shown. (B) Throw-length plot (*T-x*) for Fault 1 measured along the Top Mungaroo horizon, compared to the along-strike variation

20

in T where it abuts the fault. We restore the pre-intrusion throw profile by removing the effects of the sill thickness, assuming the sill has a seismic velocity of ~5.55(±0.555) km s^{-1}.

A *T-x* analysis of the Top Mungaroo horizon also demonstrates how the sill affects how throw varies along strike of Fault 1 (Fig. 7B; Supplementary Table 6). For example, the maximum present-day throw is ~606 m, but when the sill thickness is accounted for (i.e. we remove the sill and thus shift overlying hanging wall horizons downwards), throw increases to ~825(±22) m (Fig. 7B; Supplementary Table 6). The prominent throw minimum (present-day throw of ~269 m) on Fault 1, which disrupts the overall bell-shaped morphology of the *T-x* profile, is spatially coincident with the branch-point of the NE-SW striking hanging wall splay (Fig. 7B; Supplementary Table 6).

5 DISCUSSION

5.1 Timing of fault formation, folding, and sill emplacement

Thickening and divergence of Upper Triassic-to-Lower Cretaceous hanging wall strata towards Fault 1 indicate it was active and surface-breaking during the Late Triassic-to-Early Cretaceous (Figs 4B, C, 5, and 7A) [e.g., Jackson et al., 2017]. There are upward reductions in throw gradient and expansion indices at the Base Cretaceous unconformity, which we interpret to mark a reduction in strain rate across Fault 1 prior to deposition of the Barrow Group (Figs 4B, C, and 7A) [see also Lathrop et al., 2020]. Footwall degradation during formation of the Base Cretaceous unconformity means we cannot determine whether this reduction in strain rate locally involved a period fault cessation or not [e.g., Magee et al., 2016]. However, kinematic analyses of syn-sedimentary faults elsewhere in the Glencoe 3D seismic survey, where little or no footwall degradation occurred, suggest faulting may have been continuous during formation of the Base Cretaceous unconformity [Lathrop et al., 2020].

The top of the supra-sill fold we mapped coincides with Intra-Jurassic R2 and is onlapped by Jurassic strata beneath the Base Cretaceous unconformity (Figs 4B and 5C). Onlapping of strata onto the fold indicates Intra-Jurassic R2 represented the surface during deformation [Trude et al., 2003]. We interpret that folding occurred in response to sill emplacement and, at least partially, accommodated the intruding magma volume because: (i) strata adjacent to the fold, or beneath the sill, are not folded (e.g., Figs 4B and C), indicating deformation was not driven by regional horizontal shortening but instead by a localised, underlying, forcing process [i.e. it is a forced fold; Stearns, 1978]; (ii) folding was not driven by upwards fault propagation [e.g., Hardy and Finch, 2006], as expansion indices reveal Fault 1 was surface-breaking in the Late Triassic-to-Jurassic, prior to and likely during sill emplacement (Fig. 7A); and (iii) the lateral edge of the fold broadly overlies that of the sill (e.g., Figs 4D, E, and 5B) [e.g., Magee et al., 2019a]. We also recognise

21

depressions above the sill along Intra-Jurassic R2, which are infilled by overlying strata, and suggest these correspond to hydrothermal or volcanic vents related to sill emplacement and fluid escape (Fig. 5) [e.g., Hansen, 2006; Jamtveit et al., 2004; Planke et al., 2005]. By decompacting and backstripping the sill overburden, we estimate magma emplacement occurred in the Jurassic at a depth of ~0.9 km. Other intrusion-induced forced folds identified within the North Carnarvon

5   Basin have been dated to the Kimmeridgian, and we consider the sill-fold pair studied here are likely a similar age [e.g., Magee et al., 2013a; Magee et al., 2017].

5.2 Forced fold mechanics

Roof uplift above intrusions is typically considered to be accommodated by elastic bending of the overburden, implying

10   the volume and amplitude of ground deformation is broadly equivalent to, and thus a proxy for, the emplaced magma volume and thickness (e.g., Fig. 3A) [e.g., Bunger and Cruden, 2011; Hansen and Cartwright, 2006; Jackson et al., 2013; Pollard and Johnson, 1973; Stearns, 1978]. For example, if the deforming overburden has no flexural strength, there should be no uplift beyond the intrusion edge [e.g., Hansen and Cartwright, 2006; Magee et al., 2019a]. Although inversion of geodetic data that capture ground deformation above intrusions can produce reasonable estimates of

15   emplaced magma volumes by assuming the crust behaves elastically [e.g., Magee et al., 2018; Pritchard and Simons, 2004; Sigmundsson et al., 2020], the geometry of modelled intrusions is oversimplified compared to natural examples [Galland, 2012b]. Furthermore, field-, modelling-, and seismic-based studies demonstrate that viscoelastic and/or inelastic deformation of the overburden may accommodate magma emplacement (e.g., Fig. 3B) [e.g., Magee et al., 2013a; Magee et al., 2019a; Morgan et al., 2008; Schofield et al., 2012; Sigmundsson et al., 2020]. For example, inelastic

20   porosity reduction and faulting of the host rock can occur during bending [e.g., Magee et al., 2017; Morgan et al., 2008]. If multiple processes accommodate intrusion, as opposed to simply elastic bending, the volume of ground deformation will underestimate the intruded magma volume [Galland, 2012a]. To determine the structure of syn-emplacement ground deformation, and establish whether elastic bending solely accommodated magma intrusion, we depth-converted and decompacted the top surface of the folded sequence and compare its amplitude to sill thickness (Fig. 6). We note we

25   cannot determine whether lateral variations in compaction degree have modified the fold shape; i.e. the true F0 profile could realistically describe any pattern within the defined envelope.

Where the western limb of the fold overlies a strata-bound inclined sheet in the south of the study area, the sill is overlain by a relatively smooth, asymmetrical forced fold containing little evidence for brittle deformation (Figs 4 and 6). This

30   geometry of the western fold limb implies that here, during sill emplacement, roof uplift was accommodated by elastic bending of the overburden; this is consistent with the broad overlap between the estimated sill thickness (T) and the syn-

22

emplacement surface relief (fold amplitude F_0) around the western half of the sill (Fig. 6). We note that the fold has a present-day relief of ~50 m above the resolved western sill tip and appears to extend beyond the mapped edge of the sill (Figs 4D and 6). The maximum ST of the western inclined sill limb, which is defined by the limit of separability (56±5.6 m), is also less than the predicted F_0 range of the overlying fold (Fig. 6). These sill-fold relationships suggest: (i) the deformed strata likely had some flexural strength, meaning our decompaction method underestimates F_0 [e.g., Hansen and Cartwright, 2006; Magee et al., 2019a]; and (ii) the true sill edge is unresolved in our data.

Similar to the western side of the sill, the present-day minimum relief of the fold at Intra-Jurassic R2 above the eastern edge of the fault-hosted inclined sheet is ~47 m (i.e. the synformal fold axis); this corresponds to an estimated decompacted relief of ~48–92 m (Fig. 6; Supplementary Table 3). The amplitude of this eastern fold is also greater than the potential maximum ST of the underlying inclined sheet, which is expressed in the data as a tuned reflection package (Figs 4B and 6). However, this eastern fold limb has a synformal geometry, with a half-width of ~160 m, and is upturned immediately adjacent to Fault 1. Here, the synform has a present-day relief of ~75 m, which corresponds to an estimated decompacted relief of ~75–139 m (Fig. 6; Supplementary Table 3); i.e. F_0 does not decay to zero as is observed at the western sill limb (Fig. 6). Furthermore, we show that towards this eastern limb, the estimated range of ST is broadly greater than F_0 (Fig. 6), although we acknowledge our decompaction analysis likely underestimates F_0 as the folded section probably had flexural strength. We consider two scenarios that could produce the observed sill-fold relationships immediately adjacent to Fault 1: (i) projecting the eastward-dipping synform limb down-dip suggests F_0 may have decayed to zero at Fault 1 (i.e. the fold was a monocline, similar to that defining the western limb), implying the upturned part of the fold limb could have been generated post-folding due to normal faulting (i.e. frictional fault drag; Fig. 8A); or (ii) the synform was generated by collapse of strata during fluid escape via a pipe emanating from the sill tip (Fig. 8B), similar to hydrothermal vents observed elsewhere [e.g., Hansen, 2006; Jamtveit et al., 2004; Planke et al., 2005]. We discount the frictional fault drag mechanism because the synform shape and magnitude is inconsistent with fault dip [i.e. it is not low-angle; Grasemann et al., 2005] or geometry [i.e. it does not comprise underlapping segments; Childs et al., 2017] (Figs 4D and E). Instead we favour a fluid escape origin for the synform, which implies there may have been no prominent monoclinal limb formed above the eastern sill edge (Fig. 8B). We suggest the potential absence of a monoclinal limb above the eastern edge of the sill could be because uplift was accommodated by inversion (i.e. reverse reactivation) of Fault 1, as opposed to elastic bending (Fig. 8B). Although we favour a model involving little folding above the eastern edge of the sill, the local disparity here between F_0 and ST (Fig. 6) implies compaction of overburden strata may also have contributed to accommodating sill emplacement [Jackson et al., 2013; Magee et al., 2013a; Magee et al., 2019a].
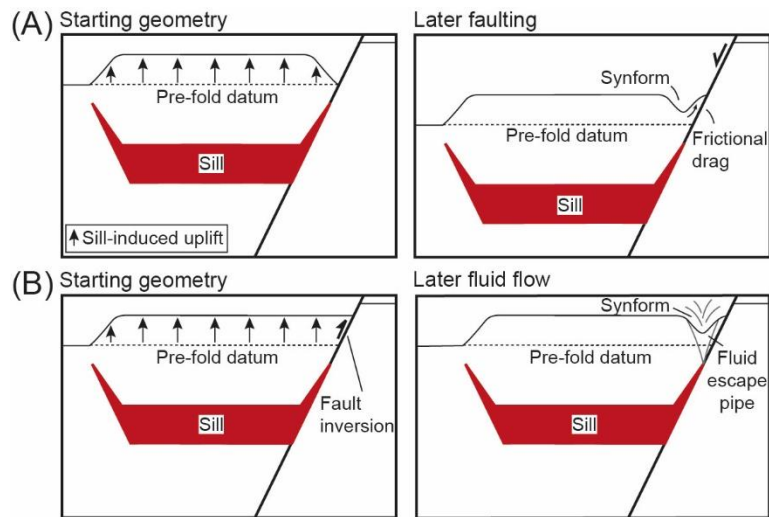
23

Figure 8: (A) Schematics showing how the synform along Intra-Jurassic R2 may be generated adjacent to Fault 1 in response to normal fault frictional drag. The fold initially extends beyond the limit of the sill and, as subsequent fault slip occurs, the fault-adjacent part of the monoclinal limb is rotated producing a synform with an axis overlying the sill tip. (B) Schematics showing how the synform along Intra-Jurassic R2 may be generated adjacent to Fault 1 by fluid expulsion from the sill tip and/or surrounding strata. In this model, there is no original monoclinal fold above the sill tip.

Overall, we suggest sill emplacement can be broadly described by a three-stage model: (i) emplacement of a thin, layer-parallel sill containing intrusive steps [Magee et al., 2019b], which spreads laterally with little or no roof uplift (Fig. 9A) [e.g., Hansen and Cartwright, 2006; Kavanagh et al., 2015; Magee et al., 2013a; Pollard and Johnson, 1973; Wilson et al., 2016]; (ii) sill inflation, which drove roof uplift and ground deformation, accommodated by elastic bending above the western part of the sill and localised inversion of Fault 1 and overburden compaction above its eastern part (Fig. 9B) [Bunger and Cruden, 2011; Galland and Scheibert, 2013; Goulty and Schofield, 2008; Magee et al., 2017; Montanari et al., 2017]; and (iii) transgression of inclined sheets, which likely exploited fold-related outer-arc extensional fractures or fault opening of Fault 1, and perhaps fluid escape (Fig. 9C) [e.g., Bedard et al., 2012; Magee et al., 2013b; Siregar et al., 2019; Thomson and Schofield, 2008]. Subsequent burial-related compaction has modified the forced fold, by reducing its amplitude (F0 becomes F), but not the thickness of the incompressible sill (Fig. 9D) [e.g., Magee et al., 2019a]. Our work confirms that the presence of pre-existing faults can, at least partly, control intrusion-induced deformation and provide pathways for magma ascent [e.g., Gaffney et al., 2007; Magee et al., 2013b; Valentine and Krogh, 2006].
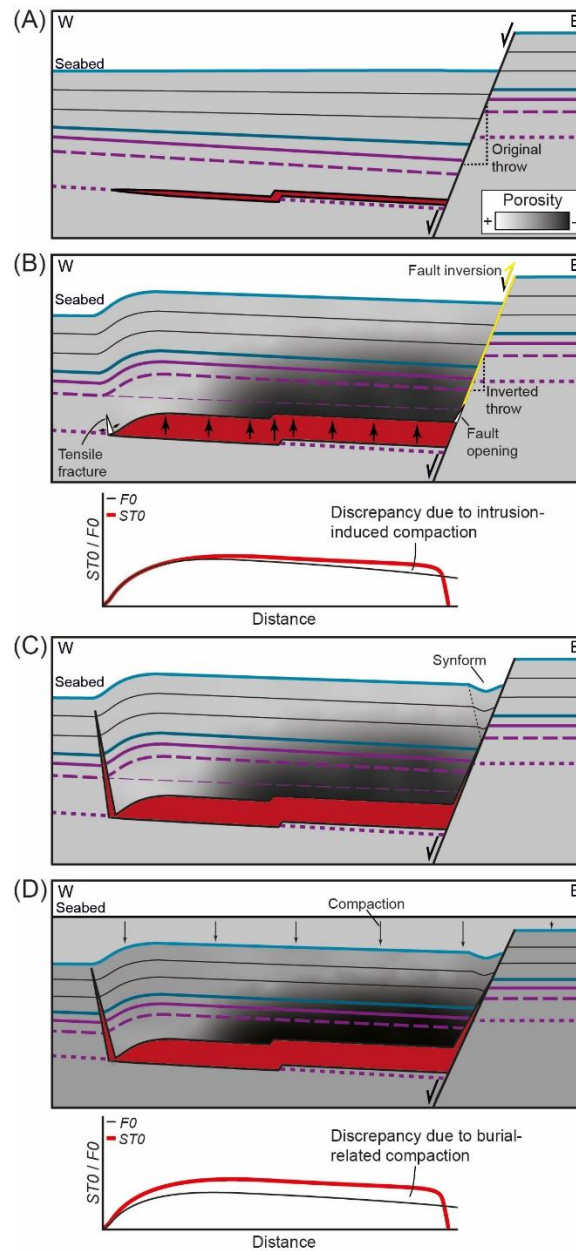
24

Figure 9: Conceptual model of inner sill and inclined sheet emplacement. (A) Intrusion and lateral propagation of a thin sill [e.g., Hansen and Cartwright, 2006; Kavanagh et al., 2015; Magee et al., 2013a; Pollard and Johnson, 1973; Wilson et al., 2016]. (B) Inflation of the sill causes uplift of the overburden, accommodated by elastic bending, particularly above the western part of the sill, and inversion of the pre-existing fault. Heterogeneous vertical compaction of the overburden also likely accommodates magma emplacement, causing a discrepancy in between *ST* and *F0* above the eastern part of the sill. Tensile fractures may open due to outer-arc stretching during folding and where the fault plane is

25

opened [Bunger and Cruden, 2011; Galland and Scheibert, 2013; Goulty and Schofield, 2008; Magee et al., 2017; Montanari et al., 2017]. (C) Magma exploits open fractures, forming inclined sill limbs [e.g., Bedard et al., 2012; Magee et al., 2013b; Siregar et al., 2019; Thomson and Schofield, 2008]. (D) Burial-related compaction reduces the forced fold amplitude but not sill thickness [e.g., Magee et al., 2019a].

5   5.3 Implications for the geometric and kinematic analysis of normal faults

Variations in throw (and displacement) across segmented normal faults is commonly interpreted to reflect their kinematics [e.g., Ferrill and Morris, 2001; Hongxing and Anderson, 2007; Needham et al., 1996; Peacock and Sanderson, 1991; Reilly et al., 2015; Robson et al., 2016; Rotevatn et al., 2019; Tvedt et al., 2013; Walsh et al., 2003; Walsh and Watterson, 1989; Watterson, 1986]. For example, numerical modelling shows the location of throw maxima may
10   coincide with the nucleation site of faults [e.g., Deng et al., 2017]. Recognition of multiple throw maxima across faults have therefore been related to the nucleation, growth, and eventual coalescence of initially isolated fault segments; in these interpretations, throw minima are inferred to represent sites of segment linkage (e.g., relay zones) [e.g., Cartwright et al., 1996; Jackson and Rotevatn, 2013; Mansfield and Cartwright, 1996; Peacock and Sanderson, 1991; Trudgill and Cartwright, 1994]. Our work shows that sill emplacement, roof uplift, and ground deformation in the immediate hanging
15   wall of a fault can drive its inversion (Fig. 8B). To demonstrate the effect such intrusion-induced inversion can have on the distribution of fault throw, we restored the original throw pattern along Fault 1 by removing the depth-converted thickness of the sill (Fig. 7). We show that Fault 1 accommodated ~15–310 m of inversion, locally producing zones of lower throw and higher throw gradients (Fig. 7). In extreme cases, where sill thickness exceeds the pre-intrusion throw on a fault, we envisage that intrusion-induced inversion could locally cause the fault to display a reverse motion.
20   Correctly identifying where intrusion-induced inversion may have modified fault throw is critical to interpreting the kinematic history of a fault. Identification of intrusion-induced inversion is likely relatively simple where sills have a clear seismic expression and their geometrical relationship to faults can be defined. However, recent studies have shown that an abundance of sub-seismic sills, i.e. with thicknesses below the limit of visibility of a seismic reflection dataset, may not be recognised but can cumulatively over-thicken a sedimentary sequence [e.g., Mark et al., 2019; Schofield et
25   al., 2017]. If the degree of over-thickening by sub-seismic sills varies across (as well as along) a fault, its throw (and displacement) distribution will be modified and poorly reflect its pre-intrusion kinematic history.

Thickening of stratigraphic packages intruded by sills may also modify expansion indices calculated across a fault. For example, in the south of our study area, the expansion index calculated between an Intra-Mungaroo and Top Mungaroo
30   is 1.59 (Fig. 7A); typically this value, which is >1, would be interpreted to indicate the fault was active and surface-breaking during deposition of this sedimentary sequence [e.g., Jackson et al., 2017]. However, if we remove the thickness

26

of the sill, then the expansion index approaches 1 (Fig. 7A). Thickness of intrusive bodies should thus be excluded from analysed of expansion indices, as failure to do so may lead to errors when determining the growth history of normal faults.

6 Conclusions

Understanding the translation of magma emplacement into ground deformation is critical to volcano monitoring, which partly relies on the inversion of surface uplift data to model intrusion geometries, locations, and volumes. Such inversions assume ground deformation occurs purely via elastic bending, but there is a growing consensus that viscoelastic or inelastic processes may also generate space for intruding magma. Using seismic reflection data from offshore NW Australia, we investigate the form of a forced fold developed above a saucer-shaped sill in the Late Jurassic. We show that elastic bending broadly accommodated emplacement; i.e. sill thickness and fold amplitude are equal across the western half of the sill. However, adjacent to a major pre-existing fault, roof uplift seems to have been suppressed (i.e. fold amplitude is less than sill thickness) and likely involved a combination of fault inversion and overburden compaction. Our results suggest that the presence of pre-existing faults can modify and complicate space generation for shallow-level intrusions, causing the true geometry and location of magma bodies to deviate from the shape and site of their surface expression. Furthermore, we demonstrate that intrusion-induced fault inversion: (i) allowed magma o ascend up the fault; and (ii) modified the displacement distribution of the fault. Given fault displacement is commonly used to unravel fault kinematics, and thereby tectonic histories, caution should be applied when interpreting fault displacement in areas where sub-seismic sills may be present.

Author contributions

JN conducted the analysis and interpretation, wrote the first paper draft, and helped edit the manuscript. CM wrote the manuscript and contributed to analysis and interpretation. CALJ and JK contributed to interpretation and manuscript editing. BL contributed to manuscript editing and understanding of the regional fault setting.

Data availability

The seismic reflection and borehole data is publicly available from https://www.ga.gov.au/nopims.

27

REFERENCES

Baudon, C., and J. Cartwright. (2008). "The kinematics of reactivation of normal faults using high resolution throw mapping". Journal of Structural Geology 30(8), pp. 1072-1084. DOI: 10.1016/j.jsg.2008.04.008

5   Bedard, J. H., H. R. Naslund, P. Nabelek, A. Winpenny, M. Hryciuk, W. Macdonald, . . . E. Girard. (2012). "Fault-mediated melt ascent in a Neoproterozoic continental flood basalt province, the Franklin sills, Victoria Island, Canada". Geological Society of America Bulletin 124(5-6), pp. 723-736. DOI: 10.1130/b30450.1

Biggs, J., E. Anthony, and C. Ebinger. (2009). "Multiple inflation and deflation events at Kenyan volcanoes, East African Rift". Geology 37(11), pp. 979-982. DOI: 10.1029/2011GC003662

10 Biggs, J., I. D. Bastow, D. Keir, and E. Lewi. (2011). "Pulses of deformation reveal frequently recurring shallow magmatic activity beneath the Main Ethiopian Rift". Geochemistry, Geophysics, Geosystems 12(9), pp. Q0AB10. DOI: 10.1029/2011GC003662

Bilal, A., K. McClay, and N. Scarselli. (2018). "Fault-scarp degradation in the central Exmouth Plateau, North West Shelf, Australia". In K. R. McClay and J. A. Hammerstein (Eds.), Passive Margins: Tectonics, Sedimentation and

15 Magmatism. (Vol. 476, pp. 231-257). London: Geological Society, London, Special Publications. DOI: 10.1144/SP476.11

Black, M., K. McCormack, C. Elders, and D. Robertson. (2017). "Extensional fault evolution within the Exmouth Sub-basin, North West Shelf, Australia". Marine and petroleum geology 85, pp. 301-315. DOI: 10.1016/j.marpetgeo.2017.05.022

20 Bunger, A. P., and A. R. Cruden. (2011). "Modeling the growth of laccoliths and large mafic sills: Role of magma body forces". Journal of Geophysical Research 116(B2). DOI: 10.1029/2010jb007648

Cannavò, F., A. G. Camacho, P. J. González, M. Mattia, G. Puglisi, and J. Fernández. (2015). "Real time tracking of magmatic intrusions by means of ground deformation modeling during volcanic crises". Scientific reports 5, 10970. DOI: 10.1038/srep10970

25 Caricchi, L., J. Biggs, C. Annen, and S. Ebmeier. (2014). "The influence of cooling, crystallisation and re-melting on the interpretation of geodetic signals in volcanic systems". Earth and Planetary Science Letters 388, pp. 166-174. DOI: 10.1016/j.epsl.2013.12.002

Cartwright, J., R. Bouroullec, D. James, and H. Johnson. (1998). "Polycyclic motion history of some Gulf Coast growth faults from high-resolution displacement analysis". Geology 26(9), pp. 819-822. DOI: 10.1130/0091-

30 7613(1998)026<0819:PMHOSG>2.3.CO;2

Cartwright, J. A., C. Mansfield, and B. Trudgill. (1996). "The growth of normal faults by segment linkage". In P. G. Buchanan and D. A. Nieuwland (Eds.), Modern Developments in Structural Interpretation, Validation and Modelling.

28

(Vol. 99(1), pp. 163-177). London: Geological Society, London, Special Publications. DOI: 10.1144/GSL.SP.1996.099.01.13

Cartwright, J. A., B. D. Trudgill, and C. S. Mansfield. (1995). "Fault growth by segment linkage: an explanation for scatter in maximum displacement and trace length data from the Canyonlands Grabens of SE Utah". Journal of Structural

5   Geology 17(9), pp. 1319-1326. DOI: 10.1016/0191-8141(95)00033-A

Castro, J. M., B. Cordonnier, C. I. Schipper, H. Tuffen, T. S. Baumann, and Y. Feisel. (2016). "Rapid laccolith intrusion driven by explosive volcanic eruption". Nature communications 7, pp. 13585. DOI: 10.1038/ncomms13585

Chaussard, E. (2016). "Subsidence in the Parícutin lava field: Causes and implications for interpretation of deformation fields at volcanoes". Journal of Volcanology and Geothermal Research 320, pp. 1-11. DOI:

10 10.1016/j.jvolgeores.2016.04.009

Childs, C., T. Manzocchi, A. Nicol, J. Walsh, A. Soden, J. Conneally, and E. Delogkos. (2017). "The relationship between normal drag, relay ramp aspect ratio and fault zone structure". In C. Childs, R. Holdsworth, C.-L. Jackson, T. Manzocchi, J. J. Walsh, and G. Yielding (Eds.), The geometry and growth of normal faults (Vol. 439, pp. 355-372). London: Geological Society, London, Special Publications. DOI: 10.1144/SP439.16

15 Childs, K., J. Banfield, M. Jakymec, and A. Jones. (2013). Well Completion Report: Chester-1 & Chester-1 ST1 interpretative data. Retrieved from National Offshore Petroleum Information Management System, Geoscience Australia.

de Saint-Blanquat, M., G. Habert, E. Horsman, S. S. Morgan, B. Tikoff, P. Launeau, and G. Gleizes. (2006). "Mechanisms and duration of non-tectonically assisted magma emplacement in the upper crust: the Black Mesa pluton,

20 Henry Mountains, Utah". Tectonophysics 428(1), pp. 1-31. DOI: 10.1016/j.tecto.2006.07.014

Deng, C., R. L. Gawthorpe, E. Finch, and H. Fossen. (2017). "Influence of a pre-existing basement weakness on normal fault growth during oblique extension: Insights from discrete element modeling". Journal of Structural Geology 105, pp. 44-61. DOI: 10.1016/j.jsg.2017.11.005

Direen, N. G., H. M. J. Stagg, P. A. Symonds, and J. B. Colwell. (2008). "Architecture of volcanic rifted margins: new

25 insights from the Exmouth – Gascoyne margin, Western Australia". Australian Journal of Earth Sciences 55(3), pp. 341-363. DOI: 10.1080/08120090701769472

Driscoll, N. W., and G. D. Karner. (1998). "Lower crustal extension across the Northern Carnarvon basin, Australia: Evidence for an eastward dipping detachment". Journal of Geophysical Research: Solid Earth (1978–2012) 103(B3), pp. 4975-4991. DOI: 10.1080/08120090701769472

30 Ebmeier, S., B. Andrews, M. Araya, D. Arnold, J. Biggs, C. Cooper, E. Cottrell, M. Furtney, J. Hickey, J. Jay, R. Lloyd, A. L. Parker, M. E. Pritchard, E. Robertson, E. Venzke & J. L. Williamson. (2018). "Synthesis of global satellite

observations of magmatic and volcanic deformation: implications for volcano monitoring & the lateral extent of magmatic domains". Journal of Applied Volcanology 7(1), pp. 2. DOI: 10.1186/s13617-018-0071-3

Eide, C. H., N. Schofield, I. Lecomte, S. J. Buckley, and J. A. Howell. (2018). "Seismic Interpretation of Sill-complexes in Sedimentary Basins: The 'sub-sill Imaging Problem'". Journal of the Geological Society 175, pp. 193-209. DOI: 10.1144/jgs2017-096

Exon, N., B. Haq, and U. Von Rad. (1992). "Exmouth Plateau revisited: scientific drilling and geological framework". Paper presented at the Proceedings of the Ocean Drilling Program, Scientific Results.

Ferrill, D. A., and A. P. Morris. (2001). "Displacement gradient and deformation in normal fault systems". Journal of Structural Geology 23(4), pp. 619-638. DOI: 10.1016/S0191-8141(00)00139-5

Frey, Ø., S. Planke, P. A. Symonds, and M. Heeremans. (1998). "Deep crustal structure and rheology of the Gascoyne volcanic margin, western Australia". Marine Geophysical Researches 20(4), pp. 293-311. DOI: 10.1023/A:1004791330763

Gaffney, E. S., B. Damjanac, and G. A. Valentine. (2007). "Localization of volcanic activity: 2. Effects of pre-existing structure". Earth and Planetary Science Letters 263(3), pp. 323-338. DOI: 10.1016/j.epsl.2007.09.002

Galland, O. (2012a). "Experimental modelling of ground deformation associated with shallow magma intrusions". Earth and Planetary Science Letters 317, pp. 145-156.

Galland, O. (2012b). "Experimental modelling of ground deformation associated with shallow magma intrusions". Earth and Planetary Science Letters 317-318, pp. 145-156. DOI: 10.1016/j.epsl.2011.10.017

Galland, O., and J. Scheibert. (2013). "Analytical model of surface uplift above axisymmetric flat-lying magma intrusions: Implications for sill emplacement and geodesy". Journal of Volcanology and Geothermal Research 253, pp. 114-130. DOI: 10.1016/j.jvolgeores.2012.12.006

Gartrell, A., J. Torres, M. Dixon, and M. Keep. (2016). "Mesozoic rift onset and its impact on the sequence stratigraphic architecture of the Northern Carnarvon Basin". The APPEA Journal 56(1), pp. 143-158.

Gibbons, A. D., U. Barckhausen, P. den Bogaard, K. Hoernle, R. Werner, J. M. Whittaker, and R. D. Müller. (2012). "Constraining the Jurassic extent of Greater India: Tectonic evolution of the West Australian margin". Geochemistry, Geophysics, Geosystems 13(5). DOI: 10.1029/2011GC003919

Goulty, N. R., and N. Schofield. (2008). "Implications of simple flexure theory for the formation of saucer-shaped sills". Journal of Structural Geology 30(7), pp. 812-817. DOI: 10.1016/j.jsg.2008.04.002

Grasemann, B., S. Martel, and C. Passchier. (2005). "Reverse and normal drag along a fault". Journal of Structural Geology 27(6), pp. 999-1010. DOI: 10.1016/j.jsg.2005.04.006

30

Guldstrand, F., S. Burchardt, E. Hallot, and O. Galland. (2017). "Dynamics of surface deformation induced by dikes and cone sheets in a cohesive Coulomb brittle crust". Journal of Geophysical Research: Solid Earth 122(10), pp. 8511-8524. DOI: 10.1002/2017JB014346

Hansen, D. M. (2006). "The morphology of intrusion-related vent structures and their implications for constraining the timing of intrusive events along the NE Atlantic margin". Journal of the Geological Society 163, pp. 789-800. DOI: 10.1144/0016-76492004-167

Hansen, D. M., and J. Cartwright. (2006). "The three-dimensional geometry and growth of forced folds above saucer-shaped igneous sills". Journal of Structural Geology 28(8), pp. 1520-1535. DOI: 10.1016/j.jsg.2006.04.004

Hardy, S., and E. Finch. (2006). "Discrete element modelling of the influence of cover strength on basement-involved fault-propagation folding". Tectonophysics 415(1-4), pp. 225-238. DOI: 10.1016/j.tecto.2006.01.002

Hocking, R. (1992). "Jurassic deposition in the southern and central North West Shelf". Western Australia: Geological Survey Western Australia Record 199217.

Hocking, R. M., H. T. Moors, and W. E. Van de Graaff. (1987). "Geology of the Carnarvon Basin, Western Australia" (Vol. 133): State Print. Division.

Hongxing, G., and J. K. Anderson. (2007). "Fault throw profile and kinematics of normal fault: Conceptual models and geologic examples". Geological Journal of China Universities 13, pp. 75-88.

Hopper, J. R., J. C. Mutter, R. L. Larson, and C. Z. Mutter. (1992). "Magmatism and rift margin evolution: Evidence from northwest Australia". Geology 20(9), pp. 853-857. DOI: 10.1130/0091-7613(1992)020<0853:MARMEE>2.3.CO;2

Jackson, C. A-L., R. E. Bell, A. Rotevatn, and A. B. Tvedt. (2017). "Techniques to determine the kinematics of synsedimentary normal faults and implications for fault growth models". In C. Childs, R. E. Holdsworth, C. A-L. Jackson, T. Manzocchi, J. J. Walsh, and G. Yielding (Eds.), The Geometry and Growth of Normal Faults. (Vol.439, pp. 187-217). London: Geological Society, London, Special Publications. DOI: 10.1144/SP439.22.

Jackson, C. A-L., N. Schofield, and B. Golenkov. (2013). "Geometry and controls on the development of igneous sill–related forced folds: A 2-D seismic reflection case study from offshore southern Australia". Geological Society of America Bulletin 125(11-12), pp. 1874-1890. DOI: 10.1130/b30833.1

Jackson, C. A-L., and A. Rotevatn. (2013). "3D seismic analysis of the structure and evolution of a salt-influenced normal fault zone: A test of competing fault growth models". Journal of Structural Geology 54(19), pp. 215. DOI: 10.1016/j.jsg.2013.06.012

Jamtveit, B., H. Svensen, Y. Y. Podladchikov, and S. Planke. (2004). "Hydrothermal vent complexes associated with sill intrusions in sedimentary basins". In C. Breitkreuz and N. Petford (Eds.), Physical geology of high-level magmatic

systems. (Vol. 234, pp. 233-241). London: Geological Society, London, Special Publications. DOI: 10.1144/GSL.SP.2004.234.01.15

Johnson, A. M., and D. D. Pollard. (1973). "Mechanics of growth of some laccolithic intrusions in the Henry mountains, Utah, I: field observations, Gilbert's model, physical properties and flow of the magma". Tectonophysics 18(3), pp. 261-309. DOI: 10.1016/0040-1951(73)90050-4

Karner, G. D., and N. W. Driscoll. (1999). Style, timing and distribution of tectonic deformation across the Exmouth Plateau, northwest Australia, determined from stratal architecture and quantitative basin modelling. In C. MacNiocall and P. Ryan (Eds.), Continental Tectonics. Geological Society, London, Special Publications (Vol. 164, pp. 271-311): Geological Society of London. DOI: 10.1144/GSL.SP.1999.164.01.14

Kavanagh, J., D. Boutelier, and A. Cruden. (2015). "The mechanics of sill inception, propagation and growth: Experimental evidence for rapid reduction in magmatic overpressure". Earth and Planetary Science Letters 421, pp. 117-128. DOI: 10.1016/j.epsl.2015.03.038

Lathrop, B., C. A.-L. Jackson, R. Bell, and A. Rotevatn. (2020). "The kinematics of growth faults and the role of lateral tip retreat". EarthArXiv pre-print. DOI: 10.31223/osf.io/ueb7r

Longley, I., C. Buessenschuett, L. Clydsdale, C. Cubitt, R. Davis, M. Johnson, N.M. Marshall, A.P. Murray, R. Somerville, T.B. Spry, and N.B. Thompson. (2002). "The North West Shelf of Australia–a Woodside perspective". The sedimentary basins of Western Australia 3, pp. 27-88.

Magee, C., F. Briggs, and C. A-L. Jackson. (2013a). "Lithological controls on igneous intrusion-induced ground deformation". Journal of the Geological Society 170(6), pp. 853-856. DOI: 10.1144/jgs2013-029

Magee, C., O. B. Duffy, K. Purnell, R. E. Bell, C. A-L. Jackson, and M. T. Reeve. (2016). "Fault-controlled fluid flow inferred from hydrothermal vents imaged in 3D seismic reflection data, offshore NW Australia". Basin Research 28(3), pp. 299-318. DOI: 10.1111/bre.12111

Magee, C., M. Hoggett, C. A-L. Jackson, and S. M. Jones. (2019a). "Burial-Related Compaction Modifies Intrusion-Induced Forced Folds: Implications for Reconciling Roof Uplift Mechanisms Using Seismic Reflection Data". Frontiers in Earth Science 7(37). DOI: 10.3389/feart.2019.00037

Magee, C., and C. A-L. Jackson. (2020). "Seismic reflection data reveal the 3D structure of the newly discovered Exmouth Dyke Swarm, offshore NW Australia". Solid Earth 11(2), pp. 576-606. DOI: 10.5194/se-2019-201

Magee, C., C. A-L. Jackson, J. P. Hardman, and M. T. Reeve. (2017). "Decoding sill emplacement and forced fold growth in the Exmouth Sub-basin, offshore northwest Australia: Implications for hydrocarbon exploration". Interpretation 5(3), pp. SK11-SK22. DOI: 10.1190/INT-2016-0133.1

Magee, C., C. A-L. Jackson, and N. Schofield. (2013b). "The influence of normal fault geometry on igneous sill emplacement and morphology". Geology 41(4), pp. 407-410. DOI: 10.1130/g33824.1

Magee, C., J. Muirhead, N. Schofield, R. J. Walker, O. Galland, S. Holford, J. Spacapan, C. A-L. Jackson, W. McCarthy. (2019b). "Structural signatures of igneous sheet intrusion propagation". Journal of Structural Geology 125, pp. 148-154. DOI: 10.1016/j.jsg.2018.07.010

Magee, C., C. T. Stevenson, S. K. Ebmeier, D. Keir, J. O. Hammond, J. H. Gottsmann, K. A. Whaler, N. Schofield, C. A-L. Jackson, M. S. Petronis, B. O'Driscoll, J. Morgan, A. Cruden, S. A. Vollgger, G. Dering, S. Micklethwaite, M. D. Jackson. (2018). "Magma plumbing systems: a geophysical perspective". Journal of Petrology 59(6), pp. 1217-1251. DOI: 10.1093/petrology/egy064

Mansfield, C. S., and J. A. Cartwright. (1996). "High resolution fault displacement mapping from three-dimensional seismic data: evidence for dip linkage during fault growth". Journal of Structural Geology 18, pp. 249-263. DOI: 10.1016/S0191-8141(96)80048-4

Mark, N., S. P. Holford, N. Schofield, C. H. Eide, S. Pugliese, D. Watson, and D. Muirhead. (2020). "Structural and lithological controls on the architecture of igneous intrusions: examples from the NW Australian Shelf". Petroleum Geoscience 26(1), pp. 50-69. DOI: 10.1144/petgeo2018-067

Mark, N., N. Schofield, D. Gardiner, L. Holt, C. Grove, D. Watson, A. Alexander, and H. Poore. (2019). "Overthickening of sedimentary sequences by igneous intrusions". Journal of the Geological Society 176(1), pp. 46-60. DOI: 10.1144/jgs2018-112

Marshall, N., and S. Lang. (2013). "A new sequence stratigraphic framework for the North West Shelf, Australia." Paper presented at the Sedimentary Basins of Western Australia 4: Proceedings PESA Symposium. Perth.

Moig N, and S. Massie. (2010). Well Completion Report, Rimfire-1, Interpretative data. Retrieved from Australia:

Montanari, D., M. Bonini, G. Corti, A. Agostini, C. J. J. o. V. Del Ventisette, and G. Research. (2017). "Forced folding above shallow magma intrusions: Insights on supercritical fluid flow from analogue modelling". 345, pp. 67-80. DOI; 10.1016/j.jvolgeores.2017.07.022

Morgan, S., A. Stanik, E. Horsman, B. Tikoff, M. de Saint Blanquat, and G. Habert. (2008). "Emplacement of multiple magma sheets and wall rock deformation: Trachyte Mesa intrusion, Henry Mountains, Utah". Journal of Structural Geology 30(4), pp. 491-512. DOI: 10.1016/j.jsg.2008.01.005

Needham, D., G. Yielding, and B. Freeman. (1996). "Analysis of fault geometry and displacement patterns". In P. G. Buchanan and D. A. Nieuwland (Eds.), Modern Developments in Structural Interpretation, Validation and Modelling. (Vol. 99(1), pp. 189-199). London: Geological Society, London, Special Publications. DOI: 10.1144/GSL.SP.1996.099.01.15

Nicol, A., J. Walsh, J. Watterson, and P. Bretan. (1995). "Three-dimensional geometry and growth of conjugate normal faults". Journal of Structural Geology 17(6), pp. 847-862. DOI: 10.1016/0191-8141(94)00109-D

33

Nicol, A., J. Watterson, J. Walsh, and C. Childs. (1996). "The shapes, major axis orientations and displacement patterns of fault surfaces". Journal of Structural Geology 18(2), pp. 235-248. DOI: 10.1016/S0191-8141(96)80047-2

Oehlers, D. J., H. D. Wright, and M. J. Burnet. (1994). "Flexural strength of profiled beams". Journal of Structural Engineering 120(2), pp. 378-393. DOI: 10.1061/(ASCE)0733-9445(1994)120:2(378)

5   Paganoni, M., J. J. King, M. Foschi, K. Mellor-Jones, and J. A. Cartwright. (2019). "A natural gas hydrate system on the Exmouth Plateau (NW shelf of Australia) sourced by thermogenic hydrocarbon leakage". Marine and petroleum geology 99, pp. 370-392. DOI: 10.1016/j.marpetgeo.2018.10.029

Paumard, V., J. Bourget, T. Payenberg, R. B. Ainsworth, A. D. George, S. Lang, H. W. Posamentier, D. Peyrot. (2018). "Controls on shelf-margin architecture and sediment partitioning during a syn-rift to post-rift transition: Insights from

10   the Barrow Group (Northern Carnarvon Basin, North West Shelf, Australia)". Earth-Science Reviews 177, pp. 643-677. DOI: 10.1016/j.earscirev.2017.11.026

Peacock, D., and D. Sanderson. (1991). "Displacements, segment linkage and relay ramps in normal fault zones". Journal of Structural Geology 13(6), pp. 721-733. DOI: 10.1016/0191-8141(91)90033-F

Planke, S., T. Rasmussen, S. S. Rey, and R. Myklebust. (2005). Seismic characteristics and distribution of volcanic

15   intrusions and hydrothermal vent complexes in the Vøring and Møre basins. In A. G. Doré (Ed.), Petroleum Geology: North-West Europe and Global Perspectives - Proceedings of the 6th Petroleum Geology Conference (Vol. 6, pp. 833-844): Geological Society, London. DOI: 10.1144/0060833

Pollard, D. D., and A. M. Johnson. (1973). "Mechanics of growth of some laccolithic intrusions in the Henry Mountains, Utah, II: bending and failure of overburden layers and sill formation". Tectonophysics 18(3), pp. 311-354. DOI:

20   10.1016/0040-1951(73)90051-6

Poppe, S., E. P. Holohan, O. Galland, N. Buls, G. Van Gompel, B. Keelson, P-Y. Tournigand, J. Brancart, D. Hollis, A. Nila, and M. Kervyn. (2019). "An Inside Perspective on Magma Intrusion: Quantifying 3D Displacement and Strain in Laboratory Experiments by Dynamic X-Ray Computed Tomography". Frontiers in Earth Science 7, 62. DOI: 10.3389/feart.2019.00062

25   Pritchard, M., and M. Simons. (2004). "An InSAR-based survey of volcanic deformation in the central Andes". Geochemistry, Geophysics, Geosystems 5(2), Q02002. DOI: 10.1029/2003GC000610

Pryer, L., K. Romine, T. Loutit, and R. Barnes. (2002). "Carnarvon basin architecture and structure defined by the integration of mineral and petroleum exploration tools and techniques". The APPEA Journal 42(1), pp. 287-309.

Reeve, M. T. (2017). The structural and stratigraphic expression of continental breakup. Imperial College London, PhD

30   Thesis.

34

Reeve, M. T., C. A-L. Jackson, R. E. Bell, C. Magee, and I. D. Bastow. (2016). "The stratigraphic record of prebreakup geodynamics: Evidence from the Barrow Delta, offshore Northwest Australia". Tectonics 35(8), pp. 1935-1968. DOI: 10.1002/2016TC004172

Reeves, J., C. Magee, and C. A. L. Jackson. (2018). "Unravelling intrusion-induced forced fold kinematics and ground deformation using 3D seismic reflection data". Volcanica 1(1), pp. 1-17. DOI: 10.30909/vol.01.01.0117

Reilly, C., A. Nicol, J. J. Walsh, and H. Seebeck. (2015). "Evolution of faulting and plate boundary deformation in the Southern Taranaki Basin, New Zealand". Tectonophysics 651, pp. 1-18. DOI: 10.1016/j.tecto.2015.02.009

Rey, S. S., S. Planke, P. A. Symonds, and J. I. Faleide. (2008). "Seismic volcanostratigraphy of the Gascoyne margin, Western Australia". Journal of Volcanology and Geothermal Research 172(1-2), pp. 112-131. DOI: 10.1016/j.jvolgeores.2006.11.013

Robb, M. S., B. Taylor, and A. M. Goodliffe. (2005). "Re-examination of the magnetic lineations of the Gascoyne and Cuvier Abyssal Plains, off NW Australia". Geophysical Journal International 163(1), pp. 42-55. DOI: 10.1111/j.1365-246X.2005.02727.x

Robson, A., R. King, and S. Holford. (2016). "Structural evolution of a gravitationally detached normal fault array: analysis of 3D seismic data from the Ceduna Sub-Basin, Great Australian Bight". Basin Research 29(5), pp. 605-624. DOI: 10.1111/bre.12191

Rohrman, M. (2013). "Intrusive large igneous provinces below sedimentary basins: An example from the Exmouth Plateau (NW Australia)". Journal of Geophysical Research: Solid Earth 118(8), pp. 4477-4487. DOI: 10.1002/jgrb.50298

Rohrman, M. (2015). "Delineating the Exmouth mantle plume (NW Australia) from denudation and magmatic addition estimates". Lithosphere 7(5), pp. 589-600. DOI: 10.1130/L445.1

Rotevatn, A., C. A.-L. Jackson, A. B. Tvedt, R. E. Bell, and I. Blækkan. (2019). "How do normal faults grow?". Journal of Structural Geology 125, pp. 174-184. DOI: 10.1016/j.jsg.2018.08.005

Schmiedel, T., O. Galland, Ø. Haug, G. Dumazer, and C. Breitkreuz. (2019). "Coulomb failure of Earth's brittle crust controls growth, emplacement and shapes of igneous sills, saucer-shaped sills and laccoliths". Earth and Planetary Science Letters 510, pp. 161-172. DOI: 10.1016/j.epsl.2019.01.011

Schmiedel, T., S. Kjoberg, S. Planke, C. Magee, O. Galland, N. Schofield, C. A-L. Jackson, D. A. Jerram. (2017). "Mechanisms of overburden deformation associated with the emplacement of the Tulipan sill, mid-Norwegian margin". Interpretation 5(3), pp. SK23-SK38. DOI: 10.1190/INT-2016-0155.1

Schofield, N., S. Holford, J. Millett, D. Brown, D. Jolley, S. R. Passey, D. Muirhead, C. Grove, C. Magee, J. Murray, M. Hole, C. A-L. Jackson, C. T. E. Stevenson. (2017). "Regional magma plumbing and emplacement mechanisms of the Faroe-Shetland Sill Complex: implications for magma transport and petroleum systems within sedimentary basins". Basin Research 29(1), pp. 41-63. DOI: 10.1111/bre.12164

35

Schofield, N. J., D. J. Brown, C. Magee, and C. T. E. Stevenson. (2012). "Sill morphology and comparison of brittle and non-brittle emplacement mechanisms". Journal of the Geological Society 169(2), pp. 127-141. DOI: 10.1144/0016-76492011-078

Sclater, J. G., and P. Christie. (1980). "Continental stretching: An explanation of the Post-Mid-Cretaceous subsidence of the central North Sea Basin". Journal of Geophysical Research: Solid Earth 85(B7), pp. 3711-3739. DOI: 10.1029/JB085iB07p03711

Sigmundsson, F., V. Pinel, R. Grapenthin, A. Hooper, S. A. Halldórsson, P. Einarsson, B G. Ófeigsson, E. R. Heimisson, K. Jónsdóttir, M. T. Gudmundsson, K. Vogfjörd, M. Parks, S. Li, V. Drouin, H. Geirsson, S. Dumont, H. M. Fridriksdottir, G. B. Gudmundsson, T. J. Wright, and T. Yamasaki. (2020). "Unexpected large eruptions from buoyant magma bodies within viscoelastic crust". Nature communications 11(1), pp. 1-11. DOI: 10.1038/s41467-020-16054-6

Siregar, E., K. O. Omosanya, C. Magee, and S. E. Johansen. (2019). "Impacts of fault-sill interactions on sill emplacement in the Vøring Basin, Norwegian North Sea". Journal of Structural Geology 126, pp. 156-174. DOI: 10.1016/j.jsg.2019.06.006

Skogly, O. (1998). Seismic characterization and emplacement of intrusives in the Vøring Basin. (M.Sc. Thesis), University of Oslo.

Smallwood, J. R., and J. Maresh. (2002). "The properties, morphology and distribution of igneous sills: modelling, borehole data and 3D seismic from the Faroe-Shetland area". In D. W. Jolley and B. R. Bell (Eds.), The North Atlantic Igneous Province: Stratigraphy, tectonic, Volcanic and Magmatic Processes (Vol. 197, pp. 271-306): Geological Society, London, Special Publications. DOI: 10.1144/GSL.SP.2002.197.01.11

Sparks, R., J. Biggs, and J. Neuberg. (2012). "Monitoring volcanoes". Science 335(6074), pp. 1310-1311. DOI: 10.1126/science.1219485

Stagg, H., M. Alcock, G. Bernardel, A. Moore, P. Symonds, and N. Exon. (2004). "Geological framework of the outer Exmouth Plateau and adjacent ocean basins". Geoscience Australia.

Stearns, D. W. (1978). "Faulting and forced folding in the Rocky Mountains foreland". Geological Society of America Memoirs 151, pp. 1-38. DOI: 10.1130/MEM151-p1

Symonds, P. A., S. Planke, O. Frey, and J. Skogseid. (1998). "Volcanic evolution of the Western Australian Continental Margin and its implications for basin development". Paper presented at the Sedimentary Basins of Western Australia 2: Proc. of Petroleum Society Australia Symposium, Perth, WA.

Thomson, K., and N. Schofield. (2008). "Lithological and structural controls on the emplacement and morphology of sills in sedimentary basins". In K. Thomson and N. Petford (Eds.), Structure and Emplacement of High-Level Magmatic Systems (Vol. 302, pp. 31-44): Geological Society, London, Special Publications. DOI: 10.1144/SP302.3

36

Thorsen, C. E. (1963). "Age of growth faulting in southeast Louisiana". Gulf Coast Association of Geological Societies Transactions 13, pp. 103-110.

Tindale, K., N. Newell, J. Keall, and N. Smith. (1998). Structural evolution and charge history of the Exmouth Sub-basin, northern Carnarvon Basin, Western Australia. Paper presented at the Sedimentary Basins of Western Australia 2: Proc. of Petroleum Society Australia Symposium, Perth, WA.

Trude, J., J. Cartwright, R. J. Davies, and J. R. Smallwood. (2003). "New technique for dating igneous sills". Geology 31, pp. 813-816. DOI: 10.1130/G19559.1

Trudgill, B., and J. Cartwright. (1994). "Relay-ramp forms and normal-fault linkages, Canyonlands National Park, Utah". Geological Society of America Bulletin 106(9), pp. 1143-1157. DOI: 10.1130/0016-7606(1994)106<1143:RRFANF>2.3.CO;2

Tvedt, A., A. Rotevatn, C. A.-L. Jackson, H. Fossen, and R. L. Gawthorpe. (2013). "Growth of normal faults in multilayer sequences: A 3D seismic case study from the Egersund Basin, Norwegian North Sea". Journal of Structural Geology 55, pp. 1-20. DOI: 10.1016/j.jsg.2013.08.002

Valentine, G., and K. Krogh. (2006). "Emplacement of shallow dikes and sills beneath a small basaltic volcanic center – The role of pre-existing structure (Paiute Ridge, southern Nevada, USA)". Earth and Planetary Science Letters 246(3-4), pp. 217-230. DOI: 10.1016/j.epsl.2006.04.031

van Wyk de Vries, B., A. Márquez, R. Herrera, J. G. Bruña, P. Llanes, and A. Delcamp. (2014). "Craters of elevation revisited: forced-folds, bulging and uplift of volcanoes". Bulletin of Volcanology 76(11), pp. 1-20. DOI: 10.1007/s00445-014-0875-x

Velayatham, T., S. Holford, M. Bunch, R. King, and C. Magee. (2019). "3D Seismic Analysis of Ancient Subsurface Fluid Flow in the Exmouth Plateau, Offshore Western Australia". Paper presented at the West Australian Basins Symposium, Perth, Western Australia.

Walsh, J., W. Bailey, C. Childs, A. Nicol, and C. Bonson. (2003). "Formation of segmented normal faults: a 3-D perspective". Journal of Structural Geology 25(8), pp. 1251-1262. DOI: 10.1016/S0191-8141(02)00161-X

Walsh, J. J., and J. Watterson. (1988). "Analysis of the relationship between displacements and dimensions of faults". Journal of Structural Geology 10(3), pp. 239-247. DOI: 10.1016/0191-8141(88)90057-0

Walsh, J. J., and J. Watterson. (1989). "Displacement gradients on fault surfaces". Journal of Structural Geology 11(3), pp. 307-316. DOI: 10.1016/0191-8141(89)90070-9

Watterson, J. (1986). "Fault dimensions, displacements and growth". Pure and applied Geophysics 124(1-2), pp. 365-373. DOI: 10.1007/BF00875732

37

Wilson, P. I., K. J. McCaffrey, R. W. Wilson, I. Jarvis, and R. E. Holdsworth. (2016). "Deformation structures associated with the Trachyte Mesa intrusion, Henry Mountains, Utah: Implications for sill and laccolith emplacement mechanisms". Journal of Structural Geology 87, pp. 30-46.

Yang, X.-M., and C. Elders. (2016). "The Mesozoic structural evolution of the Gorgon Platform, North Carnarvon Basin, Australia". Australian Journal of Earth Sciences 63(6), pp. 755-770.

5